UNIVERSITY OF LATVIA

Summary of Doctoral Thesis

Artis Aberfelds

RESEARCH OF 6.7 GHZ METHANOL MASERS: OBSERVATION METHODS, MONITORING AND SOURCE MORPHOLOGY

Riga 2024

UNIVERSITY
OF LATVIA

FACULTY OF PHYSICS, MATHEMATICS AND OPTOMETRY

Artis Aberfelds

RESEARCH OF 6.7 GHZ METHANOL MASERS: OBSERVATION METHODS, MONITORING AND SOURCE MORPHOLOGY

SUMMARY OF THE DOCTORAL THESIS

Submitted for the Doctoral Degree in Natural Science,
Field: Physics and astronomy
Subfield: Astrophysics and Fundamental Astronomy

Riga 2024

The doctoral thesis was carried out: at the Chair of Faculty of Physics, Mathematics and Optometry of University of Latvia and the Research Institute ”Ventspils International Radio Astronomy center” of Ventspils University of Applied Sciences (VIRAC) from 2014 to 2023.
The thesis contains the introduction, reference list, literature review, methods, two chapters of results and closing remarks. Form of the thesis: dissertation in physics, subdisciple of astrophysics and fundamental astronomy.

Supervisor: Dr. Phys. Ivar Shmeld, lead researcher.
Reviewers:

1) Dr. Phys. Ilgmārs Eglītis;
2) Dr. Phys. Alberto Sanna;
3) Dr. Phys. Kazi Lucie Jessica Rygl.

The thesis will be defended at the public session of the Doctoral Committee of the Doctoral Committee of Physics, Astronomy and Mechanics University of Latvia, at 22 March 2024 15:00, Jelgavas str. 3.
The thesis is available at the Library of the University of Latvia, Kalpaka blvd. 4.

This thesis is accepted for the commencement of the degree of Doctor of Natural Science on by the Doctoral Committee of of Physics, Astronomy and Mechanics Universitvia _____

Chairmen of Doctoral Committee _____

Secretary of the Doctoral Committee _____

ISBN 978-9934-36-194-4
ISBN 878-9934-36-195-1 (PDF)

Abstract

Massive stars significantly influence their surrounding environment. They are capable of ionizing interstellar gas, creating HII regions, and in the final stages of their evolution, exploding as supernovae, enriching the surroundings with heavy elements. Additionally, their intense luminocity shapes the appearance of galaxies by forming spiral arms.

Despite their importance, the formation of massive stars remains a challenging topic. The growth of mass beyond the Eddington limit continues to be an active subject of research. The large distances and absorption by gas and dust pose significant obstacles to their observation in their early evolutionary stages. This is where second-class methanol masers, especially at 6.7 GHz, start to play a crucial role, as they are exclusivly found in regions of massive star formation.

Using very long baseline interferometry (VLBI), it was determined that most methanol masers are located in the environment that flows toward the disk and follows its rotation.

In this work, the author monitored 42 such sources and conducted in-depth studies of three sources, obtaining and analyzing their radio images.

As part of the doctoral thesis, the restored Irbene radio telescopes were adapted for cosmic maser observations. A four-step frequency shift method was introduced, and a set of computer programs for data reduction was developed.

The author compiled the results of methanol maser monitoring over five years, obtaining 42 source variability time series. These series exhibit various types of variability and relative amplitudes. For some sources, significant changes in the trends of brightness variations were observed during the monitoring period. Additionally, periodic flux oscillations are potentially detected in three sources.

As part of the thesis work, the author applied for and obtained the opportunity to observe three sources with the European VLBI Network (EVN), obtaining millisecond-resolution images. Two sources were observed with this resolution for the first time. The obtained images reveal long-standing maser cloudlets, which, in the context of the acquired time series, support the hypothesis of variability being linked to changes in pumping radiation intensity. The evolution of the maser spots indicates dynamic processes in the environment. In the case of G78.122+3.633, differences in morphology and variability were noted between groups of spots associated with the disk or the interaction zone between the disk and outflowing gas.

Contents

1 General description

1.1 Relevance and motivation

The development of stellar evolution theories is one of the most significant achievements in 20th-century astronomy. Investigating the processes of star formation posed particular challenges, as these processes occur in optically opaque clouds. While a simple theory can describe the formation of stars like the Sun and lower-mass stars, explaining the formation of high-mass stars remains problematic.

The processes that enable a star to continue accumulating mass during the accretion process are a current focus of research in modern astronomy. A significant portion of observational programs with leading instruments worldwide is dedicated to these studies. The most recent and pertinent results indicate the nonlinearity of these processes, suggesting that they occur rapidly on astronomical timescales, even with catastrophic events. Presently proposed theories are unable to predict these rapid accretion events. Consequently, the only way to detect and study these events is through monitoring.

In this regard, the role of second-class 6.7 GHz methanol masers, found exclusively in these objects, becomes essential. Past results indicate that maser emission is significantly influenced during accretion outbursts, with a positive correlation between the star and maser emission intensity. Coordinated observations organized by informal maser monitoring groups have allowed the detection of one to three such events per year. Maser signals are narrowband and intense, making them well-suited for monitoring with medium-class radio telescopes like those at the Ventspils International Radio Astronomy Centre (VIRAC) in Latvia.

This work presents five-year-long time series data for forty-two methanol masers, including their flux densities. Three of these sources were observed using the European Very-Long-Baseline Interferometry Network (EVN), producing milliarcsecond-resolution radio images. The morphology of these sources is described, as well as potential causes of maser variability. Additionally, the solutions developed for adapting the Irbene Radio Telescopes for maser observations are outlined.

1.2 The aims and the task for the thesis

The aim of this work is to investigate the activity of second-class 6.7 GHz methanol masers, particularly their variability, in the context of massive star formation processes.

The following tasks were set for the implementation of the work:

- Adapt the Irbene Radio Telescopes for maser observations;
- Select suitable sources for a long-term monitoring program;

- Conduct a systematic long-term observation campaign;
- Collect and analyze the obtained maser flux density time series;
- Obtain individual source images observed with an interferometer;
- Analyze the obtained images in the context of the acquired time series.

1.3 Novelty

The results obtained in the work are of scientific novelty and have been published in several anonymously reviewed international journals. The most important results of the work are as follows:

- Adaptation of the Irbene Radio Telescopes for maser observations;
- Obtained time series of flux density variations for 42 maser sources;
- First-time acquisition of mili-arcsecond precision images of two maser regions;
- Detailed analysis of the properties of individual maser features and cloudlets;
- Identification of the relationship between the location of maser features around a star and their variability.

1.4 Author contribution

The preparation of the radio telescopes for maser observations was carried out in close collaboration with the engineering team of the Ventspils International Radio Astronomy Centre (VSRC). The author was responsible for observation planning and formulating the requirements for the aperture configuration. The author conducted all data processing and interpretation presented in the work. The results of the work have been presented at 7 international conferences and published in 11 anonymously reviewed publications, of which the author is the corresponding author for four. Most of the observations were performed by the telescope operators at VSRC. Jānis Šteinbergs assisted in creating data processing scripts. During the interferometer data processing and interpretation, the author was mentored by Anna Bartkiewicz and Marian Szymczak.

1.5 Methods

For maser line observations with the Ventspils International Radio Astronomy Centre (VSRC) radio telescopes, we chose the four-step frequency switching method as the most suitable. A total of 42 sources were selected for the methanol

maser monitoring program, and they were observed at least once a week. We obtained time series of source flux density spanning 5 years. Three sources, located near the sky, were selected for the European Very Long Baseline Interferometry Network (EVN) application to obtain milliarcsecond-resolution radio images.

1.6 The approbation of scientific results

1.6.1 Scientific publications

1. A Aberfelds, J Šteinbergs, I Shmeld, R. Burns, Five years of 6.7 GHz methanol maser monitoring with Irbene radio telescopes, Monthly Notices of the Royal Astronomical Society, Volume 526, Issue 4, December 2023, Pages 5699–5714, https://doi.org/10.1093/mnras/stad3158

2. A Aberfelds, A Bartkiewicz, M Szymczak, J Šteinbergs, G Surcis, A Kobak, M Durjasz, I Shmeld, Milliarcsecond structure and variability of methanol maser emission in three high-mass protostars, Monthly Notices of the Royal Astronomical Society, Volume 524, Issue 1, September 2023, Pages 599–618, https://doi.org/10.1093/mnras/stad1752

3. R. A. Burns, Y. Uno, N. Sakai, J. Blanchard, Z. Rosli, G. Orosz, Y. Yonekura, Y. Tanabe, K. Sugiyama, T. Hirota, Kee-Tae Kim, A. Aberfelds, A. E. Volvach, A. Bartkiewicz, A. Caratti o Garatti, A. M. Sobolev, B. Stecklum, C. Brogan, C. Phillips, D. A. Ladeyschikov, D. Johnstone, G. Surcis, G. C. MacLeod, H. Linz, J. O. Chibueze, J. Brand, J. Eislöffel, L. Hyland, L. Uscanga, M. Olech, M. Durjasz, O. Bayandina, S. Breen, S. P. Ellingsen, S. P. van den Heever, T. R. Hunter, X. Chen, A Keplerian disk with a four-arm spiral birthing an episodically accreting high-mass protostar. Nat Astron 7, 557–568 (2023). https://doi.org/10.1038/s41550-023-01899-w

4. Aberfelds, A ; Šteinbergs, J ; Shmeld, I. ; Bartkiewicz, A. , A preview look at the maser cloudlet evolution in the HMSFR IRAS 20126+4104, in Euro-Asian Astronomical Society, Astronomical and Astrophysical Transactions, Vol. 32, No. 4.., Cambridge Scientific Publishers, Coll. Astronomical and Astrophysical Transactions, France, ISBN : 9781908106827, pp. 383-388, doi : https://doi.org/10.17184/eac.5655

5. Svetlana V Salii, Igor I Zinchenko, Sheng-Yuan Liu, Andrej M Sobolev, Artis Aberfelds, Yu-Nung Su, The methanol emission in the J1– J0 A−+ line series as a tracer of specific physical conditions in high-mass star-forming regions, Monthly Notices of the Royal Astronomical Society, Volume 512, Issue 3, May 2022, Pages 3215–3229, https://doi.org/10.1093/mnras/stac739

6. Tomoya Hirota, Pawel Wolak, Todd R Hunter, Crystal L Brogan, Anna Bartkiewicz, Michal Durjasz, Agnieszka Kobak, Mateusz Olech, Marian

Szymczak, Ross A Burns, Artis Aberfelds, Giseon Baek, Jan Brand, Shari Breen, Do-Young Byun, Alessio Caratti o Garatti, Xi Chen, James O Chibueze, Claudia Cyganowski, Jochen Eislöffel, Simon Ellingsen, Naomi Hirano, Bo Hu, Ji-hyun Kang, Jeong-Sook Kim, Jungha Kim, Kee-Tae Kim, Mi Kyoung Kim, Busaba Kramer, Jeong-Eun Lee, Hendrik Linz, Tie Liu, Gordon MacLeod, Tiege P McCarthy, Karl Menten, Kazuhito Motogi, Chung-Sik Oh, Gabor Orosz, Andrey M Sobolev, Bringfried Stecklum, Koichiro Sugiyama, Kazuyoshi Sunada, Lucero Uscanga, Fanie van den Heever, Alexandr E Volvach, Larisa N Volvach, Yuan Wei Wu, Yoshinori Yonekura, Millimeter methanol emission in the high-mass young stellar object G24.33+0.14, Publications of the Astronomical Society of Japan, Volume 74, Issue 5, October 2022, Pages 1234–1262, psac067

7. Antyufeyev, O. ; Bleiders, M. ; Patoka, O. ; Bezrukovs, V. ; Aberfelds, A. ; Shmeld, I. ; Orbidans, A. ; Steinbergs, J. ; Karelin, Y. ; Shukga, V. (2022), Receiver gain and system temperature instability during the calibration of spectral data at radio telescopes in C-band, in Euro-Asian Astronomical Society, Astronomical and Astrophysical Transactions, Vol. 33, No. 2.., Cambridge Scientific Publishers, Coll. Astronomical and Astrophysical Transactions, France, ISBN : 9781908106865, pp. 113-122, doi : https://doi.org/10.17184/eac.6474

8. Šteinbergs, J ; Aberfelds, A ; Bleiders, M ; Shmelds, I., VIRAC maser data processing suite, Astronomical and Astrophysical Transactions, Vol. 32, No. 3..,pp. 227-240, Cambridge Scientific Publishers, Coll., France, doi : https://doi.org/10.17184/eac.5643 , (2021)

9. O. Patoka, O. Antyufeyev, I. Shmeld, V. Bezrukovs, M. Bleiders, A. Orbidans, A. Aberfelds, V. Shulga, New ex-OH maser detections in the northern celestial hemisphere, DOI: 10.1051/0004-6361/202037623, A&A 652 A17 (2021)

10. M. Bleiders, O. Antyufeyev, O. Patoka, A. Orbidans, A. Aberfelds, J. Steinbergs, V. Bezrukovs and I.Shmeld, Spectral Line Registration Backend Based on USRP X300 Software Defined Radio, Journal of Astronomical Instrumentation, Volume 9, Issue 2, id. 2050009-773, (2020)

11. Antyufeyev, O. ; Bleiders, M. ; Patoka, O. ; Bezrukovs, V. ; Aberfelds, A. ; Shmeld, I. ; Orbidans, A. ; Steinbergs, J. ; Shulga, V., Estimation of errors at the calibration of spectral data at the Irbene RT-32 radio telescope, Astronomical & Astrophysical Transactions, Issue 1, Vol. 32, p. 23-38, (2020)

12. Aberfelds, A., Shmeld, I., & Berzins, K. (2017). Long term 6.7 GHz

methanol maser monitoring program. Proceedings of the International Astronomical Union, 13(S336), 277-278.

1.6.2 Other publications

- Burns, R. A. ; Kobak, A. ; Garatti, A. Caratti o. ; Tolmachev, A. ; Volvach, A. ; Alakoz, A. ; Wootten, A. ; Bisyarina, A. ; Dzodzomenyo, A. ; Sobolev, A. ; Bartkiewicz, A. ; Aberfelds, A. ; Stecklum, B. ; Kramer, B. ; Macdonald, C. ; Cyganowski, C. ; Paco, C. ; Garcia Miro, C, Recent updates on the Maser Monitoring Organisation, European VLBI Network Mini-Symposium and Users' Meeting 2021, 12-14 July, 2021

- J. Steinbergs; A. Aberfelds; V. Bezrukovs; K. Skirmante; A. Orbidans; I. Shmeld and R.A. Burns, Single-baseline interferometer for mJy observations, European VLBI Network Mini-Symposium and Users' Meeting 2021, 12-14 July, 2021

1.6.3 Participation in international conferences

- A. Aberfelds, K. Berzins and I. Shmeld, Initial methanol maser measurements with VIRAC RT32 Irbene radio telescope, Young European Radio Astronomers Conference (YERAC), Bonn, Germany (2016)

- A. Aberfelds, K. Berzins and I. Shmeld, Long term methanol maser monitoring program, Internacional Astronomy Uninon (IAU) 336. symposium Astrophysical Masers: Unlocking the Mysteries of the Univers, Kaljari, Italy (2017)

- A. Aberfelds and I. Shmeld, First year of 6.7 GHz methanol maser monitoring, European Week of Astronomy and Space Science (EWAS 2018), Liverpool, Great Brittany (2018)

- A. Aberfelds and K. Berzins and I. Shmeld, Metanol maser observations with Ventspils radio telescopes, Space physics, Yekaterinburg, Russia (2019)

- A. Aberfelds, Two year results of methanol maser monitoring program by Irbene radio telescopes, 6th Gamow International Conference in Odessa: "New Trends in Astrophysics, Cosmology and Radioastronomy after Gamow" un 19th Gamow Summer School: "Astronomy and beyond: Astrophysics, Cosmology, Radioastronomy and Astrobiology, Odessa, Ukraine (2019)

- A. Aberfelds and I. Shmeld, Cloudlet evolution in IRAS 20126+4104 during last 15 years and its periodic variability, 15th European VLBI Network (EVN) Symposium and the EVN Users Meeting "15th EVN Symposium", Cork, Ireland (2022)

- A. Aberfelds, A. Bartkiewicz, M. Szymczak, J. Šteinbergs and I. Shmeld, New insides of 6.7 GHz methanol maser variability in IRAS 20126+4104, International Astronomical Union Symposium 380 Cosmic Masers: Proper Motion toward the Next-Generation Large Projects, Kagoshima, Japan (2023)

1.6.4 Scientific projects

- "Physical and chemical processes in the interstellar medium", No 1.1.1.11/6A/213 supported by ERDF (ASTRA), 2017 - 2020 (molecular maser line observations)
- Latvian Council of Science Project "Organic matter evolution in stars and planets forming regions" Nr.: lzp-2018/1-0170 (LZP OMG), 2018 - 2021; (various molecule observations around HMYSOs)
- Latvian Council of Science Project "Research of Galactic Masers" Nr.: lzp-2018/1-0291 (LZP GMP), 2018 - 2021 (maser observations and monitoring using single-dish mode)
- "A single-baseline radio interferometer in a new age of transient astrophysics" Nr.:lzp-2022/1-0083 (LZP IVAR), 2023-2026; (HMYSOs monitoring with single-baseline radio interferometer)
- "Multi-Wavelength Study of Quasi-Periodic Pulsations in Solar and Stellar Flares" Nr.: lzp-2022/1-0017 (LZP STEF), 2023-2026; (Single-baseline radio interferometer use for observing M-dwarf flares)

1.7 Structure of the thesis summary

The work investigates methanol maser activity. The summary includes a literature review on massive star formation and cosmic maser phenomena. In the methodology section, the application of the Ventspils International Radio Astronomy Centre (VSRC) radio telescopes for maser observations is described. The main scientific results are divided into two sections, the first one concerning maser monitoring results, and the second one about the milliarcsecond-resolution studies of three sources with the European Very Long Baseline Interferometry Network (EVN).

2 Literature review

2.1 Astrophysical masers

2.1.1 Introduction

The terms *"laser"* and *"maser"* originate from the English acronyms: *"light amplification by stimulated emission of radiation"* and *"microwave amplification by stimulated emission of radiation"*. The diversity of the Universe has created conditions for these phenomena to manifest in nature as well. In this overview, we won't delve into the physical aspects determining the existence of stimulated emission and the initiation of an active medium. From the observer's perspective, stimulated emission radiation manifests as significantly increased light flux in wavelengths where stimulated emission transitions occur.

Overall, masers have been found in various celestial objects, including comets in our Solar system, young star-forming nebulae, late-stage stellar envelopes, and galactic cores.

Historically, the first maser signal was detected in 1965 by one group (Weinreb et al., 1965), while another group independently conducted similar observations (Gundermann, 1965). The first known source was W49, a massive star-forming region, where hydroxyl radical (OH) transition radiation at 1665 MHz frequency was observed.

In the literature review, we will provide a concise overview of second-class 6.7 GHz methanol masers, their variability characteristics, potential causes, and massive star formation.

2.1.2 6.7 GHz methanol masers

Methanol (CH_3OH) is the most complex molecule in which maser emission has been observed throughout the Universe. Significantly, the various methanol masers have a correlation between their excitation mechanisms (collisions or radiation) and the evolutionary stage of the maser source. Accordingly, masers excited by collisions belong to the first class (Class I), while those excited by radiation belong to the second class (Class II).

Of all the observed methanol maser transitions, $5_1 \rightarrow 6_0A^+$ is the brightest. This transition, with a frequency of 6668519200 Hz (6.7 GHz), was first observed in 1991 (Menten, 1991). The association of maser-containing objects with OH masers, ultra-compact HII regions, and previously known bright 12 GHz methanol $2_0 \rightarrow 3_{-1}E$ masers indicates their affiliation with second-class YSO (young stellar object) objects. Subsequent observations have only reinforced the initially observed association, and today, second-class 6.7 GHz methanol masers are exclusively linked to massive star formation (Breen et al., 2013).

It is believed that the pumping radiation for second-class masers does not originate from the methanol molecules themselves. Dust grains, which serve as

frequency down-conversion converters for the star's ultraviolet (UV) radiation, are considered the most likely source of the thermal radiation.

Studies of methanol maser kinematics (van der Walt, D. J. et al., 2007) have shown that the radial velocity values correspond well to the disk's rotation around the star according to Kepler's laws. However, the directions of the maser linear structures and their orientation with respect to the magnetic field are ambiguous (De Buizer, J. M. et al., 2009) regarding the disk model. Most of the known 6.7 GHz methanol masers are oriented perpendicular to the disk, indicating alignment with a jet. As models develop, a significant portion of the known 6.7 GHz methanol masers is associated with material flowing onto the disk (Vlemmings et al., 2010). Pestalozzi, M. R. et al. (2009), analyzing NGC 7538, concluded that maser regions can also be located at the boundary between the disk and the outflow.

2.1.3 Variability

The first reports of variability in 6.7 GHz methanol masers came from extensive sky surveys. A notable study was conducted by Caswell et al. (1995), who observed 245 sources at four- to five-month intervals over a 1.5-year period. They concluded that 75% of maser lines remained relatively stable, with only 25% of observed lines exhibiting significant (by factor of two) intensity variations. Similar variations in amplitude were observed in just $5-7\%$ of the sources from the sample of 972 in the methanol multi-beam survey (Breen et al., 2015).

To date, two major surveys of methanol maser variability have been conducted by teams from South Africa (Goedhart et al., 2004) and Poland (Szymczak et al., 2017). The South African team initially monitored 54 sources for 4.2 years, with observation frequencies ranging from 2 to 4 times per month, and in some cases, daily. The Polish team surveyed 166 sources 2 to 4 times a week, collecting data over 3.7 years. Both teams found that approximately 81% and 79% of the monitored sources, respectively, can be considered variable.

Despite monitoring a smaller number of masers, Goedhart et al. (2004) was the first to identify all the common types of variability. They discovered sources that monotonically increased or decreased observed flux, exhibited irregular amplitude fluctuations, experienced short- and long-term flares, and most notably, detected periodic flux variations. Goedhart et al. (2004) identified seven sources with periods ranging from 132 to 520 days.

To characterize the flux variations of the obtained spectral lines in a more meaningful way, it is reasonable to use statistical indicators. In their studies, both Goedhart et al. (2004) and Szymczak et al. (2017) employed the variability index (VI) as one of these parameters. This statistical tool for describing variable stars was introduced by Stetson (1996). For the analysis of maser variability, a

modified formula (1) introduced by Aller et al. (2003) is more convenient to use.

$$VI = \frac{(S_{max} - \sigma_{max}) - (S_{min} + \sigma_{min})}{(S_{max} - \sigma_{max}) + (S_{min} + \sigma_{min})} \tag{1}$$

Where S_{max} and S_{min} represent the maximum and minimum flux density, and σ_{max} and σ_{min} represent their respective uncertainties. For spectral lines with a constant flux, the variability index (VI) approaches zero, while highly variable sources tend to have a VI close to one. Unfortunately, for weak sources with similar flux values and uncertainties, this tool can yield negative values. Moreover, since only two characteristic values are used from the entire set of variability, VI is sensitive to gross errors.

Therefore, a better tool for characterizing variability is the fluctuation index (FI), which was also recommended by Aller et al. (2003). The fluctuation index essentially measures the dispersion of data around the median value (2).

$$FI = \left[\frac{N}{\sum_{i=1}^{N} \sigma_i^2} \left(\frac{\sum_{i=1}^{N} S_i^2 \sigma_i^2 - \overline{S} \sum_{i=1}^{N} S_i \sigma_i^2}{N-1} - 1 \right) \right]^{0.5} / \overline{S} \tag{2}$$

Where S_i is the individual flux density value in measurement i, $\overline{S}$ is the median flux density value, σ_i is the uncertainty in the specific measurement, and N is the number of observations. Similarly to the variability index, the fluctuation index tends to approach zero for less variable sources, but there is no upper limit to the value of FI.

$$\chi_r^2 = \frac{1}{N-1} \sum_{i=1}^{N} \left(\frac{S_i - \overline{S}}{\sigma_i} \right)^2 \tag{3}$$

Finally, let's include the χ_r^2 test (3), also known as the reduced chi-square statistic or Mean Squared Weighted Deviation (MSWD). This statistic characterizes the goodness of fit of the constant flux density model to the observed flux variations. For a source with a constant flux density, the χ_r^2 value tends towards one.

2.1.4 Periodicity

With the discovery of periodic methanol masers, theorists began proposing models to explain this phenomenon. Typically, strictly periodic variations in radiation are explained by the presence of a close binary star system at the center. One such model is the colliding-wind binary (CWB) model. Ionizing particles or photons resulting from the collision of stellar winds disrupt the usual equilibrium when they reach the boundary between ionized and non-ionized gas, creating additional photons. Due to orbital motion, the position where this additional ioniza-

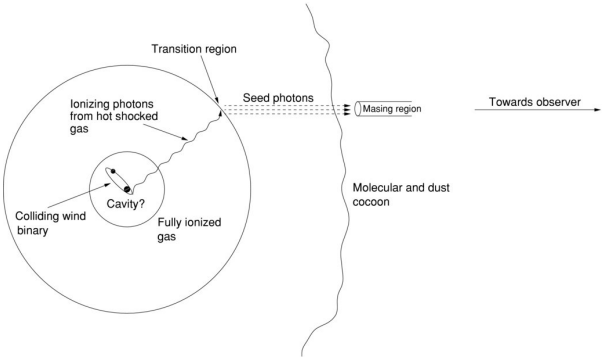

Figure 1: Colliding-wind binary (CWB) inducing maser variability (van der Walt, 2011)

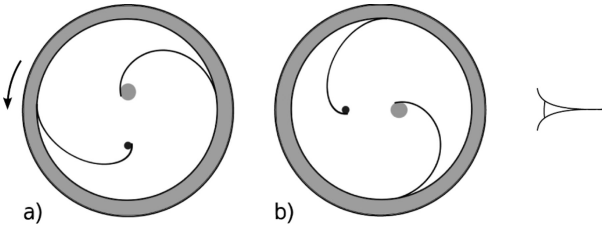

Figure 2: Binary pair of stars with surrounding disk and spiral arms in it. Here two states are showed with half or orbital period difference, arrow points in direction of rotation.(Parfenov and Sobolev, 2014)

tion radiation reaches changes periodically. These periodic changes in position at the boundary of the HII region correspondingly induce maser variability (see Figure 1) (van der Walt, 2011).

Alternatively, Araya et al. (2010) proposed a model in which a binary star system modulates the accretion rate through orbital mechanics. Periodically, it draws in more material, which alters the intensity of radiation.

Similarly, orbital mechanics can lead to the formation of shocks in the disk, specifically shock waves resembling spiral arms in galaxies (Parfenov and Sobolev, 2014). In this case, the disk's shock features follow the orbital motion of stars and can periodically encounter active maser regions, supplying them with more than the usual amount of pumping photons (see schematic in Figure 2).

On the other hand, Inayoshi et al. (2013) modeled the radiation from stars during active accretion and found that under sufficiently rapid processes, pulsations can be observed. Mechanical oscillations occur in the He layer under the influence of the κ process, similar to other variable stars.

2.1.5 Flares

Special attention is also paid to scenarios where a very rapid increase in maser brightness is observed. Here, we are talking about a multiple times increase in radiation intensity within a short period of time, resulting in significant changes in the source's spectrum to the point of being unrecognizable. Flaring can involve all observed spectral components or just one individual line.

As the simplest flaring model, we will consider the overlap of active masing regions (referred to as cloudlets in this work). From the general theory, we already know that the observed maser intensity is proportional to the depth of the active medium when two independent regions, due to their motion, align on a straight line with the observer. In such cases, a significant increase in the observed radiation intensity can occur. This effect was first described by Elitzur (1992), and it explains well the observed flares in Orion KL, for example (Shimoikura et al., 2005).

The active medium is in local thermodynamic equilibrium where a fraction of molecules is in higher energy states. Initially, the population proportions are mainly dependent on the intensity of the stimulating radiation. Until saturation is reached, when additional pumping energy can no longer increase the number of stimulated molecules. It's noted that unsaturated masers are significantly more variable than saturated ones. The alignment of unsaturated maser cloudlets on one axis can result in an exponential increase in radiation intensity.

A much more impressive type of maser flare is associated with an accretion flare, when the central star rapidly accretes a significant amount of material (from Jupiter's mass to a significant fraction of the Solar mass) over a short period. The first such 6.7 GHz methanol maser flare was discovered by Fujisawa et al. (2015), who regularly monitored the S255IR-NIRS3 (abbreviated as S255) source, and several new spectral lines were discovered, with their brightness increasing rapidly. Subsequent observations in the near-infrared range showed a significant increase in brightness from the central object and the polar outflow regions, confirming the occurrence of an accretion flare (Uchiyama et al., 2019). By comparing past VLBI observations with those obtained during the flare, Moscadelli et al. (2017) concluded that the previously observed active maser regions had disappeared, and new ones had appeared further from the central star.

2.2 The Formation of Massive Stars

2.2.1 Introduction

Massive stars form in dense and optically opaque clouds through the gravitational collapse process. Although this process is well understood, there is still uncertainty about the mechanisms that allow for the formation of objects of such diverse masses, particularly high-mass stars ($M>8\ M_{\odot}$). Stellar statistics indicate

that massive stars form relatively infrequently, but their impact on galaxy evolution is significant. They contribute to the production of a variety of chemical elements, create ionization zones (HII regions), and play a dominant role in the formation of spiral arms in galaxies.

2.2.2 YSO classification

Infrared observations of a large number of young stellar objects (YSOs) were classified into four classes based on their spectral properties by Lada and Wilking (1984). They introduced the spectral index α (4), where λ represents the wavelength and F_λ is the flux, as a qualitative indicator of the amount of radiation emanating from a heated protoplanetary disk (Lada, 1987).

$$\alpha = \frac{dlog(\lambda F_\lambda)}{dlog\lambda} \tag{4}$$

Class 0 the most early evolution phase, undetectable λ <20μm.

Class I sources have positive spectral indexes (typically α>0.3), most intense in mm and sub – mm wavelengths.

Class II -0.3>α>-1.6, objects start to be optically observable, they have height excess mid and near infrared emission originating from protoplanetary disk. Typical object in this evolution stage are T Tauri stars.

Class III α<-1.6, spectra approaches the black body profile, star incrementally louses surrounding dense disk and becomes main sequence star in Hertzsprung – Russell diagram.

2.2.3 Collapse and accretion of massive stars

The collapse of a protostar (a stage in stellar evolution when radiation energy comes from gravitational contraction) can be easily described by a model that balances radiation pressure and gravitational force. The duration of this process can be determined using the Helmholtz-Kelvin relationship 5, where τ_{HK} represents the collapse time, G is the gravitational constant, M is the protostar's mass, R is its radius, and L is the protostar's luminosity.

$$\tau_{HK} = \frac{GM^2}{2RL} \tag{5}$$

Using the empirical relationship between radiation energy and stellar mass $L \propto M^{3.2}$, and the relationship between size and mass $R \propto M^{0.6}$, the collapse time can be estimated as $\tau_{HK} \propto M^{-1.8}$. Comparing this time scale for a protostar of solar mass and 10 $M_\odot$, we obtain approximately 10^7 and 10^5 years, respectively. The typical accretion rate is estimated to be 10^{-5} $M_\odot$/year, so comparing τ_{HK} with τ_{acc} leads to the conclusion that for stars with masses M>8 $M_\odot$, the collapse ends before the

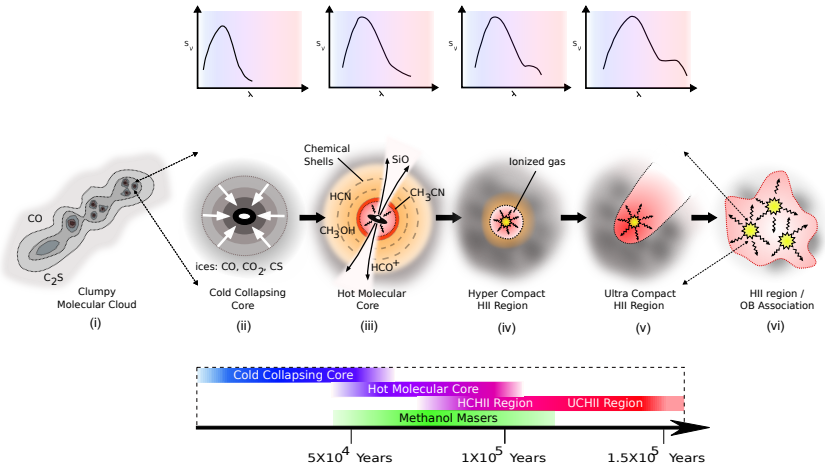

Figure 3: The illustration depicts the most plausible evolution scenario for a massive star cluster. The numbering corresponds to the central row, starting from the left edge. The four panels in the middle show the individual object evolution, while the two outer panels represent the cluster as a whole. (i) Massive stars form in dense and cold gas and dust clumps located in giant molecular clouds. (ii) These clumps fragment and become cores, gravitational forces allow them to gain mass through core merging or accretion. This stage corresponds to Class 0 and Class I young stellar objects. (iii) Heat and gas outflows from the central proto-star evaporate ice from dust grains, promoting a rich and time-varying chemical process that creates complex hydrocarbon compounds. This stage corresponds to Class II YSO. (iv) The young stars' ultraviolet radiation creates hyper-compact HII (HCHII) regions, which expand and over time destroy complex chemical compounds. This stage corresponds to Class III YSO. (v) The ionization zone has grown and become an ultra-compact HII (UCHII) region, and thermal radio radiation is easily observable. (vi) As the ultra-compact zones grow, they encounter other massive star UCHII regions, forming an HII region - OB association. The upper panel shows the radiation spectrum of an individual source at various stages of evolution, including additional infrared emissions from the disk. The lower panel shows the timescale for various evolutionary processes and the period during which second-class methanol masers (including 6.7 GHz) can exist in these objects. (Purcell, 2007)

accretion process, and nuclear fusion reactions begin before accretion is complete. Based on these estimates, two significant conclusions can be drawn regarding the differences between low-mass and high-mass star formation: high-mass stars do not have the pre-main sequence stage, and once the collapse is completed, a high-mass star is *"born"* as an O or B-type main sequence star.

OB stars have high temperatures and luminosity, which creates a substantial radiation pressure on the gas and dust in the protoplanetary disk. This dynamics can be examined using the Eddington limit, which represents the balance between gravitational (equation 6) and radiation-induced (equation 7) pressures.

$$\frac{dp}{dr} = -G\frac{M\rho}{r^2} \tag{6}$$

$$\frac{dp}{dr} = -\frac{k\rho}{c}\frac{L}{4\pi r^2} \tag{7}$$

Where ρ is gas density, r – distance from mass center, k – optical dept and c – speed of light respectfully. In the case of ionization k=σ_T/m_p, where σ_T is Thomson dispersion radius and m_p mass of proton. So the Eddington limit can be expressed as fallows (8).

$$L_{Edd} = \frac{4\pi GMm_pc}{\sigma_T} = 3.2\times10^4\left(\frac{M}{M_\odot}\right)\mathrm{L}_\odot \tag{8}$$

Stars whose luminosity exceeds the Eddington limit ($L > L_{\mathrm{Edd}}$) are unstable, and mass loss occurs due to the radiation pressure. Typically, this effect becomes significant when the mass of the star exceeds 30 $\mathrm{M}_\odot$, resulting in a mass loss of $10^{-4} - 10^{-3}$ $\mathrm{M}_\odot$ per year.

From the aforementioned and in detailed numerical simulations (Vorobyov and Basu, 2006), it is clear that monotonous accretion alone cannot form massive stars. Therefore, the formation of massive stars cannot be simply described by scaling up models that explain the formation of low-mass stars (Zinnecker and Yorke, 2007). In their review, Zinnecker and Yorke (2007) summarized the ideas explaining this mystery, and the proposed models can be broadly grouped into three classes.

The monotonic collapse model, modified to have significantly much more a dense, turbulent, and fragmentary (clumpy) disk. In essence it is based on scaling up the standard star formation model, but with a much greater emphasis on the role of the disk, which is sufficiently dense and optically thick and can efficiently shadow central object, allowing for continued mass growth. Such calculations have been performed by Vorobyov and Basu (2006), demonstrating that there can be periods (shorter than 100 years) when the accretion rate can be significantly (at least 10 times) faster than the typical rate.

Observations have shown (Brandl et al., 1996) that massive stars form in the

dense centers of star-forming regions, typically in clusters that later evolve into open star clusters. Lower-mass star-forming cores are found throughout the volume of the cloud. In their study, Bate and Bonnell (2005) demonstrated that the central cores of young stars, influenced by the collective gravitational field, are capable of accret a larger amounts of gas, allowing for more efficient mass growth compared to cores on the periphery of the cloud. Collectively, these models could be referred to as "competitive accretion."

Stellar merger model (Coagulation) is also proposed. As the name suggests, this model considers the formation of massive stars as a result of the merger of two or more lower-mass protostars. For example, Bally and Zinnecker (2005) explain observations in the core of the Orion Nebula, OMC-1, using this model. However, studies by Dale and Davies (2006) indicate that such collisions are quite rare, with only about 0.1 percent of massive stars experiencing stellar mergers. Although the cores of densest star-forming regions could have a sufficiently high density ($> 10^8 M_{\odot} pc^{-3}$) to account for the large population of massive binary stars.

2.2.4 Gas ionization

As massive stars compresses, they become hot enough for their radiation to ionize the gas, forming hyper-compact and then ultra-compact HII regions. Hyper-compact HII regions are small, about 0.01 pc, and dense, with ionized gas clouds of around $n_H \sim 10^6\ cm^{-3}$. These regions intensely emit thermal radio radiation. It is believed that these regions are associated with individual, recently formed OB-class stars. It's essential to note that during this stage of evolution, the star's gravitational attraction and accretion flows can still dominate over radiation and stellar wind pressure, preventing hyper-compact HII regions from growing hydrodynamically. This is valid until the growth rate of hyper-compact HII regions becomes less than the sound speed ($\sim 10\ km\ s^{-1}$) in the ionized gas (closed HII region model).

A pertinent question is whether the presence of ionized gas only slows down the star's mass growth, as ions are known to strongly "feels" the magnetic field and can reduce the gas's angular momentum, increasing the accretion rate. As the central OB-class star gains mass, the radiation increases, and inevitably, the critical point is reached when the HII region's expansion overcomes gravitational center-directed forces. Then, rapid HII region expansion begins, destroying the proto-star's disk and scattering the surrounding gas, making the star optically observable. The typical radius of the HII region is so large that it ionizes the gas in other small and large mass star-forming groups, significantly affecting their further evolution.

All the processes mentioned above are summarized in Figure 3, which shows the timescale of massive star formation, with all the critical stages.

3 Methods

3.1 Introduction

The Earth's atmosphere is transparent to waves with wavelengths shorter than 20 meters (approximately 15 MHz) but longer than 0.2 mm (approximately 1.5 THz). This range is known as the radio window. As radio waves have much longer wavelengths than visible light, the achievable resolution using similar-sized primary mirrors is much lower. Therefore, most radio telescopes can only detect radiation from celestial sources as point-like objects. The majority of the collected radiation in the telescope comes through the main beam, which forms a spatial angle towards the sky. The flux of radiation from a source is measured in Jansky (1 Jy = 10^{-26} W m^{-2} Hz^{-1}).

During observations, a radio telescope not only records the signal from the source but also the system's internal noise. To remove this noise, various methods of internal (instrumental) signal recording have been developed. Two of the most widely known methods are position switching (moving the primary beam of the telescope away from the source) and frequency switching (changing the frequency band that the receiver detects).

3.2 Situation overview in Irbene complex

The Ventspils International Radio Astronomy Center (VIRAC) has a rather interesting and unusual history, which will not be fully reflected in this work. From the perspective of the research presented here, the complex reconstruction in 2014 and 2015 marked the threshold after which scientific studies using the instruments at the Ventspils Radio Telescopes could be conducted. The optical characteristics of both antennas were restored, sensitive wideband receivers were procured and installed, and a modern telescope control system was introduced.

The desire to conduct research related to massive star formation, based on the capabilities of VIRAC's instruments, led to the conclusion that the most productive direction was observations of 6.7 GHz Class II methanol masers. However, for these observations to yield scientifically valuable data, preparatory work needed to be done. The reconstruction and equipping of the telescopes did not include funding for the necessary equipment for such observations, and additional funding was not available. Therefore, in close collaboration with the institute's technical staff, methods were developed to adapt existing equipment for use in spectral line observations.

This task was implemented in several stages. Initially, in trial observations, spectra were recorded using the laboratory's spectrum analyzer. Subsequently, automated observations were carried out using second-generation Digital Baseband Converters (DBBC2), and finally, a Software Defined Radio (SDR) was used.

3.3 Frequency switching method with SDR

Both telescopes use the Ettus Research USRP X300 as the spectral recorder. Transitioning to Software Defined Radio (SDR) significantly eased the load on the institute's data servers. During observations, real-time Fast Fourier Transform (FFT) is performed, which means that if with the DBBC2, a 15-minute observation of a single source took up approximately 1.5 GB of disk space, and further FFT was needed to obtain the spectrum, the SDR stores only about 8.5 MB. The SDR is also more sensitive than the DBBC2, primarily because it digitizes data using a 14-bit signal level resolution (DBBC2 effectively uses only 2 bits).

Regular calibration sessions are conducted by observing long-term stable quasars, providing reference points for system sensitivity evaluations. In this regard, invaluable support is provided by scientists from the Very Large Array (VLA) in the United States, whose source flux density estimates are also used by us. An important system parameter that requires external information for estimation is the elevation-dependent antenna temperature and flux density unit, expressed as Degrees Per Flux Units (DPFU). For RT-32, it is 0.0857 K Jy^{-1}, and for RT-16, it is 0.046 K Jy^{-1} at the zenith. Their variation as a function of telescope elevation is described by a third-order polynomial approximation.

Observations are conducted with a predetermined set of necessary parameters contained in the source configuration record, as exemplified in Table 1. Typical observational parameters for maser monitoring include a 1.5625 MHz bandwidth and 4096 FFT channels, which correspond to a spectral resolution of 0.017 km s^{-1}. During line observations, a telescope control script generates a unique "*.log" file that contains essential information about the observation settings and the telescope's operations during the observation.

In maser and other line observations, a frequency switching method is used, which is described in detail and recommended by Winkel et al. (2012). The calibration involves four steps. In the first two steps, the local oscillator frequency is symmetrically shifted (offset) by $1/2^N$ (N - positive integers, most commonly 1/4) of the bandwidth with the noise diode turned off, denoted as sig_{off} and ref_{off} (abbreviated as s0 and r0), and the same frequency shift is applied when recording data with the noise diode on, denoted as sig_{on} and ref_{on} (abbreviated as s1 and r1). The noise diode signal level T_{cal} is known and is the same for both telescopes, equal to 3.820791 K. Each of these steps is saved in a file containing three data columns with the respective frequency and amplitude for both polarizations. The data records are stored in a unique folder, the name of which is created based on the source name, frequency, station designation, and observation sequence number (e.g., `cepa_f6668_ib_1292`), where the aforementioned data files are located (e.g., `cepa_f6668_ib_1292_no001r0.dat`).

Observations are reduced using the institute-developed software suite: Maser Data Processing Suite (MDPS). For a more detailed description of the software used for spectral data processing, please refer to the code and documentation

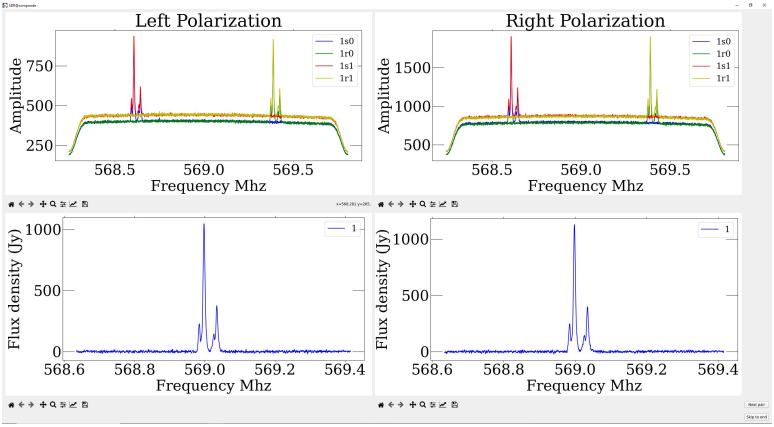

Figure 4: The MDPS script `sdr_fs.py` workspace. The right and left sides display the processing of the right and left circularly polarized signals, respectively. In the upper panel, the FFT spectrum of the four calibration steps is shown, each frame in a different color. In the lower panel, the calibrated spectrum after the execution of the algorithm is displayed.

by Šteinbergs et al. (2021) available on the GitHub repository[1]. An example of MDPS operation is shown in Figure 4.

3.4 Error evaluation

A significant aspect of measurement precision is the targeting or positioning of the telescope on the source, known as pointings. By performing a large number of amplitude measurements using the position switching method, the average pointing offset from the real source position can be determined. For RT-16, this offset is 0.033^o or 2 arcminutes, which approximately corresponds to 92% of the normalized amplitude.

Amplitude errors are determined by the uncertainty of the telescope gain, which depends on elevation and system temperature. The uncertainty of the system temperature (T_{sys}) for the Irbene Radio Telescopes is small, as shown by measurements conducted by Antyufeyev et al. (2022). Under good weather conditions, it's around 1%, but during rain or when there are heavy clouds, it increases to 1 - 3%. On the other hand, the gain varies significantly, and in seasons with high humidity and heavy rainfall, the scatter of time series is significant. By analyzing time series of barely changing sources and comparing their daily values to median values, the relative uncertainty of amplitudes is estimated. Particularly high uncertainty occurs during the winter season, significantly increasing the determined value to 20%.

[1] https://github.com/sklandrausis/Maser-Data-Processing-Suite

Table 1: Maser observation with SDR backend configuration

Configuration entry example	explanation
[g78p12_f6668]	configuration header; includes note to rest frequency
source = g78p12	source short title
RA=20h14m26.05839s	Source Right ascension (ICRS J2000)
DEC= 41d13m32.5278s	Source Declination (ICRS J2000)
v_rad = -7.1	Source radial velocity, km s^{-1}
lo = 6100	Local oscillator frequency, MHz
n_scans = 15	repetition number
cal_interval = 1	Calibration interval
t_int = 15	Duration of calibration step, s
bw_num = 3	band with
ns = 4096	FFT channels
raw_flag = 0	Option to save raw data
win = 2	FFT window method
fov = 1	FFT window overlapping
df_div = 4	Local oscillator frequency change step

3.5 Author contribution

The preparation of the telescopes for work with a new observation methodology is a labor-intensive process that cannot be achieved by one person alone. This process involved the following individuals, each of whom made a significant contribution: Mārcis Bleiders, Artūrs Orbidāns, and Jānis Šteinbergs. Mārcis Bleiders was responsible for maintaining and calibrating the electronics of both telescopes, ensuring their technical readiness, and providing substantial assistance in implementing the methodology. Artūrs Orbidāns managed the observatory's computer networks and control computers. He was in charge of automating the practical aspects of observations and managing the generated data. Jānis Šteinbergs played a major role in the practical programming of MDPS and maintained its repository. The author formulated the data acquisition algorithm, selected the most suitable calibration algorithm, conducted quality tests, and developed data processing procedures. He also created prototypes of scripts and algorithms for result compilation.

4 Monitoring of 6.7 GHz methanol masers

4.1 Introduction

Methanol maser monitoring is one of the most significant scientific activities at the Ventspils International Radio Astronomy Institute. As mentioned earlier, these sources are closely linked to the formation of massive stars, which remains an active research area in astronomy. Methanol masers serve as important indicators of the processes involved in the birth of high-mass stars. While detailed interferometric data are needed for in-depth studies of individual objects, valuable insights into their evolution are provided by changes in their spectra.

The methanol maser monitoring program was initiated in March 2017. A total of 42 sources were selected, with declinations above -10 degrees and flux densities exceeding 3 Jy. Each source was observed at intervals of 3 to 5 days, but in cases where flux density changed rapidly, daily observations were conducted.

Our monitoring results are regularly presented at meetings of the methanol maser monitoring organization. We first introduced this program during the International Astronomical Union (IAU) Symposium 336.

4.2 Observations

The observational methodology and its gradual improvements were discussed in the previous section. As the target masers are located in the Galactic plane, this determines the most suitable times for conducting observations. Due to the orbital motion of Earth, this time gradually changes. In practice, observations and the determination of suitable times are carried out by telescope operators. This is based on the number of selected sources and the sources we wish to observe each day. Observations are conducted for approximately 14 to 17 hours per week, which corresponds to 800 to 1200 hours per year, and a total of over 6000 hours over the entire program. The majority of observations, around 97%, are conducted using RT-16, primarily because RT-32 is still undergoing modernization.

4.3 Results

The light curves of flux variations for 42 selected sources were obtained, indicating changes in radiation over time at different radial velocities. Based on this data, it is possible to classify the variability of sources and determine their statistical parameters. Statistical parameters are showed for only three of the selected sources (see Table 2). Here, V_P (km s^{-1}) represents the radial velocity of the spectral line relative to the Local Standard of Rest (LSR), S_P (Jy) is the median flux density of spectral components, and VI and FI are the variability and fluctuation indices. χ^2_r is a parameter, MJD_s indicates the starting day of observations in

Modified Julian Days (number of days starting from November 17 1858), T_S represents the duration of the light curves in years, N is the number of observations, and C (month^{-1}) is the average observation frequency per month.

4.3.1 Characterization of variability in selected sources for EVN observations.

Statistical values of variability are summarized in Table 2. The obtained light curves of sources are shown in Figure 5.

G78.122+3.633. All the features in G78.122+3.633, except for the -6.1 km s^{-1} feature, are moderately or highly variable. The feature at -7.7 km s^{-1} has the highest variability indices (Table 2). It initially had a flux density of 32 Jy but decayed to $\sim$1.5 Jy after 1.6 yr and remained at a noise level over $\sim$1.5 yr, then increased to 105 Jy at the end of our monitoring. The other variable features essentially show a similar pattern of variability. The -6.1 km s^{-1} feature decreased by about 25 per cent on a timescale of 5.5 yr, which is marginally above the measurement accuracy. The high cadence observations after MJD 59045 revealed, for the variable features, the occurrence of flux fluctuations by a factor of 0.7$-$3.5 on a timescale range of 9$-$40 d imposed on the overall growth of flux on a timescale of 2.2 yr. We conclude that the fluctuations are real because their amplitudes are well above the measurement uncertainty. The Lomb-Scargle periodogram analysis (Scargle, 1982) showed no statistically significant periodicity for these fluctuations. These relatively rapid fluctuations are simultaneous within 3$-$4 d.

G90.925+1.486. The two main features in G90.925+1.486 are moderately variable (Table 2). A likely flare occurred around MJD 58250 when the flux density increased by a factor of two during 58 d, but the flare profile could not be determined due to a gap in observations. One can only notice that the flux density has returned to a pre-flare level after 7.5 months. Since MJD $\sim$58570 the emission shows an overall decrease by a factor of 1.5 during $\sim$3 yr. There are similar changes in the intensity of the two features on timescales 3$-$11 months, but their amplitudes are within or below uncertainty in the absolute flux density calibration.

G94.602−1.796. The emission of G94.602$-$1.796 is faint and not significantly variable within the noise.

4.4 Discussion

We have conducted extensive flux monitoring for forty-two 6.7 GHz methanol masers, spanning up to five years. During the observing program, we noticed various maser variability types. The summary of source variability by types, described below.

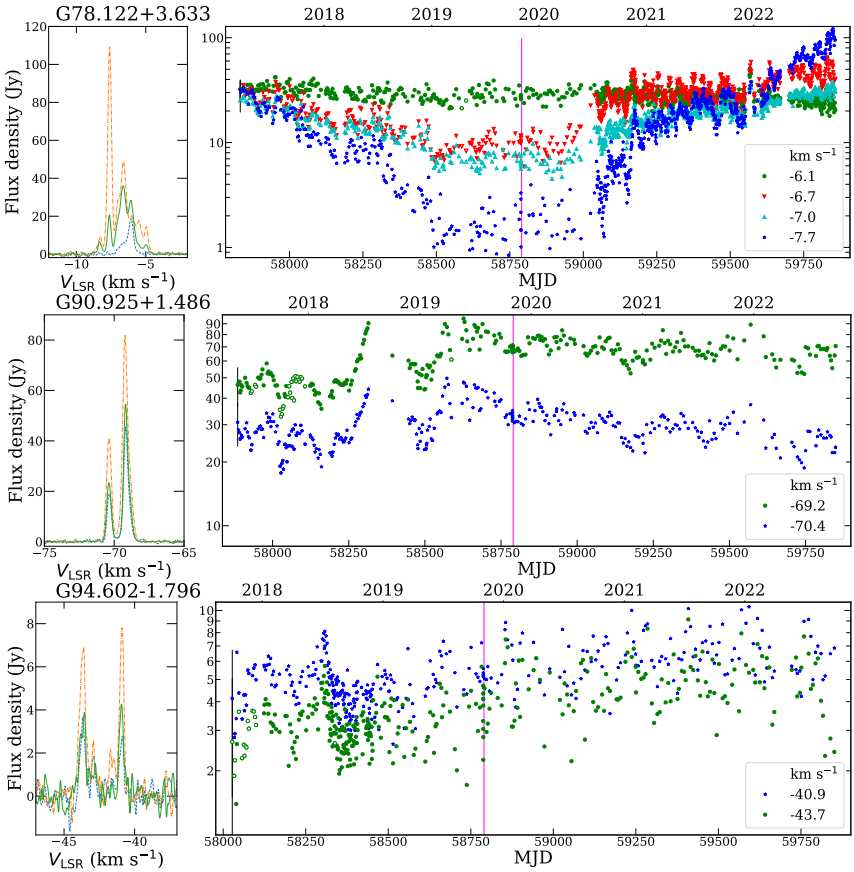

Figure 5: Spectra and light curves of the 6.7 GHz maser emission in the studied objects. Left-hand panels: maximum (orange), minimum (blue) and average (green) spectra. Right-hand panels: light curves of main features. The filled and empty symbols represent the data from the 16-m and 32-m telescopes, respectively. Typical measurement uncertainty is shown by the bar for the first data point. The vertical magenta line denotes the date of EVN observations.

Table 2: Variability properties of selected features.

V_P(km s^{-1})	S_P(Jy)	VI	FI	χ^2_r
G78.122+3.633 (MJD$_s$=57832 T_s= 5.549,				
N=882, $C(month^{-1})$=13.247)				
-6.1	27.70	0.24	0.20	0.61
-6.7	29.15	0.74	0.67	11.66
-7.0	18.42	0.62	0.64	4.87
-7.7	24.06	0.97	2.48	65.51
G90.925+1.486 (MJD$_s$=57885 T_s= 5.379,				
N=305, $C(month^{-1})$=4.725)				
-69.2	61.49	0.36	0.44	3.99
-70.4	29.79	0.37	0.39	1.60
G94.602-1.796 (MJD$_s$=58027 T_s= 4.996,				
N=351, $C(month^{-1})$=5.854)				
-40.9	5.30	0.14	0.45	0.68
-43.0	2.88	0.73	0.26	0.43
-43.7	3.74	0.43	0.47	0.59

Low–variable. We categorise a maser source as having low variability when the variability indexes for all its spectral components are below 0.25. In this category are 21 per cent sources from our sample.

Moderately variable. The variability index of the most variable component falls between 0.26 and 0.5. This variability type constitutes 26 percent of all sources.

Highly variable. A source is classified as highly variable if the variability index of at least one of its spectral components is above 0.5. This criterion was met for 55 percent of the sources in our study.

Correlated fluctuations. In this category, sources with two or more spectral features whose variability time series show a high (>0.7) positive correlation coefficient. Only sources with notable variability (variability index >0.25) are considered, we found that 19 per cent of sources have this variability type.

Anti–correlated fluctuations. Similar to the above but for spectral features exhibiting high (<-0.7) negative correlation coefficient. For example: in G33.641-0.228 the feature pair at 59.6 and 59.3 km s^{-1} are anti-correlated with features at 63.2 and 62.7 km s^{-1}; in G109.871+2.114/Cepheus A, the feature at -2.1 km s^{-1} is strongly anti - correlated with features at -3.7, -4.0 and -4.7 km s^{-1}. Only 7 per cent of our sources have this type of variability.

Velocity drifting. Refers to a continuous change in the radial velocity of a spectral line, with a drift of at least several spectral channels (>0.07 km s^{-1}) of the observed maximum velocity of the line. In our sample, only a single source (G121.298+0.659), or 2 percent, exhibited this kind of behaviour.

Cyclical variability. Periodic oscillations were observed in 19% of the se-

lected sources. Parameters of the periodic sources are summarized in Table 3. It provides approximate period length, the number of observed cycles, the typical flux change range (from minimum to maximum), relative flux increase from the minimum, and references to literature sources where the periodic signal of the source was first mentioned.

Raising. A source is considered to be rising if its flux density steadily increases by more than 50 percent over a period of 100 days. We observed this rising flux trend in 7 percent of the sources in our sample.

Falling. Similarly, if a spectral feature steadily loses flux by more than 50 percent in less than 100 days, we classify it as a falling flux source. We observed this type of flux decrease in 10 percent of sources. Importantly, there is a significant overlap between the rising and falling flux sources, where the flux density of the same spectral components alternately and steadily increases or decreases.

Flaring. As mentioned before a flare is a rapid increase in maser flux density. We propose identifying a flux increase as a flare when the flux density exceeds above a rolling mean flux and five times the statistical standard deviation of the flux within that time span. More details on our flare definition are given in Section 4. If the period of increased flux extends beyond 25 days, we further classify it as a **long flare**. Conversely, if the flux returns to its usual levels in less than 25 days, we categorize it as a **short flare**. After a flare, we see that the flux usually returns to its pre-flare intensity, but the rise and decline profiles of flare are often source-distinctive, as noted by Szymczak et al. (2017). We detected flaring activity in 10 percent of the sources in our sample.

A significant advantage of using the Irbenes complex for the monitoring program is the ability to obtain much denser observations. In our study, 21% of all sources meet the criteria for being classified as not highly variable, and this does not significantly differ from the results of 19% in Goedhart et al. (2004) and 21% in Szymczak et al. (2017). The most significant difference lies in the proportion of highly variable components, but this can be explained by the source selection process. Primarily selected bright sources often tend to be less variable (Szymczak et al., 2017). Quantitatively, our results align with Goedhart et al. (2004) and Szymczak et al. (2017). A comparison of monitoring programs is presented in Table 4.

Eight of the observed sources exhibit quasi-periodic flux fluctuations (Table 3). Most of them were already known and mentioned in the literature. We also identified three potentially periodic signals that were not reported in the literature: G192.60-0.05 at -6.3 km s^{-1}, G32.04+0.06 at 92.7 km s^{-1}, and G33.641-0.228 at 61.0 km s^{-1}. It's worth noting that in these sources, periodic variations occur in only one spectral line, which is relatively less common than periodic variations in all components. Additionally, their relative flux increase (the percentage by which the maximum flux exceeds the minimum) is relatively smaller compared to the periodically changing sources documented in the literature. The

Table 3: Parameters of periodic (cyclical) sources. The variation range displays the typical minimum and maximum flux densities within a cycle. In the case of several spectral lines following the same periodic pattern, we utilized the parameters of the most intense lines. The relative increase indicates the percentage by which the minimum amplitude increased during the cycle.

Source	Approximate Period days	Observed number of cycles	Variation range (Jy)	Relative Increase (%)	Reference
G22.357+0.066	170	9.2	11-37	240	Szymczak et al. (2011)
G32.04+0.06	57	11	108-200	90	This work
G33.641-0.228	500	4.4	5-55	100	Olech et al. (2019)
G33.641-0.228	115	7	40-95	130	This work
G37.55+0.20	250	5.2	3-13	330	Araya et al. (2010)
G73.06+1.80	123	5	4-14	250	Szymczak et al. (2015)
G192.60-0.05	235	5.5	60-120	100	This work
G196.454-01.67	110	7	5-32	600	Szymczak et al. (2017)
G107.298+5.63	34.4	43	*-250	$> 2.5 \times 10^4$	Szymczak et al. (2016)

* Flux regularly fell bellow our detection level.

longest period observed among the sources is 500 days (G33.641-0.228). However, literature mentions longer periods for G33.641-0.228, G196.454-01.67, and G188.95+0.89/S252 (Goedhart et al. 2004; Olech et al. 2019), yet in our obtained time series data, longer periods were not identified with a high degree of confidence. The shortest period observed is 34.4 days for G107.298+5.639. Sources exhibiting ascending and descending flux changes may potentially turn out to be periodic over a longer timeframe. To confirm this hypothesis, longer time series of flux variations for these sources are required.

The average values of the obtained variability descriptors for the studied sources are as follows: a variability index of 0.33, a fluctuation index of 0.54, and a χ_r^2 parameter of 4.66. The highest determined variability index value is 0.99, a fluctuation index of 6.76, and a χ_r^2 parameter of 308. These values were only observed in various components of G107.298+5.63. This suggests that G107.298+5.63, which exhibits periodic flaring, is the most variable source in the group of monitored sources. Most of the variable sources with a high variability index ($VI >$ 0.5) have low or moderate flux density. Similar correlations are also observed between the source's flux, FI, and χ_r^2 parameters. There is a positive correlation between the variability index, the fluctuation index, and the χ_r^2 parameter.

4.5 Author contribution

The author selected the sources included in the program, familiarized themselves with and reviewed the necessary literature sources, developed and implemented the data acquisition methodology, and conducted a significant number of observations, especially in the program's first two years. These responsibilities were later taken over by the telescope operators as the implementation process concluded, and the system, as a whole, became stable and ready for other users. Data processing and interpretation are also part of the author's responsibilities. In collaboration with Jānis Šteinbergs, computer programs for time series man-

Table 4: Comparison with the studies by Goedhart et al. (2004) [1]; Szymczak et al. (2017) [2] and Sugiyama et al. (2019) [3].

	[1]	[2]	[3]	This work
Start of monitoring program	Jan 1999	Jun 2009	Dec 2012	Mar 2017
End of the examined period	Mar 2003	Feb 2013	Nov 2016	Oct 2022
Duration of monitoring (yr)	4.2	3.7	3.9	5.3
Number of sources	54	137	442	42
Percentage of sample overlap to ours	24	90	97	-
Average observation cadence per month	2-4	1	6-8	6.5
Percentage of periodic sources	13	7	10	19
Percentage of high variable features	55	54	*	28
Percentage of low-variable sources	19	21	*	21

* Unknown value

agement were created. Scripts for data visualization and periodic signal searches were also developed. The obtained results have been summarized, interpreted, and subsequently published in the MNRAS journal, with the author being the first and corresponding author of this publication.

5 EVN observations

5.1 Sources

In collaboration with scientists from the Department of Radio Astronomy at Nicolaus Copernicus University, an application was created to use the EVN (European Very Long Baseline Interferometry Network). Three variable sources from the monitoring program were selected for which the following criteria were met: they have not been observed with the EVN recently, and their angular separation is not too large. The following sources were chosen:

G78.122+3.633. Widely known as IRAS 20126+4104, it hosts an impressive protoplanetary disk surrounding a central $\sim 7M_{\odot}$ B0.5 star (Cesaroni et al., 1997). Using VLBI techniques, Moscadelli et al. (2011) reported on the structure of 22 GHz water masers in outflows and two groups of 6.7 GHz methanol masers, with partially overlapping VLSR values (-4.5 to -8.5 km s^{-1}). Based on measurements of peculiar motion and magnetic field (Surcis et al., 2014), it was concluded that the first group resides in the infalling gas flow of the disk, while the second group is located in the region of interaction between the disk and the jet flow. Recent parallax measurements give a value of 0.645±0.030 mas, corresponding to a distance of $1.6^{+0.3}_{-0.12}$ kpc (Reid et al., 2019). A review by Hu et al. (2016) reveals methanol maser emission ranging from -8.43 to -4.74 km s^{-1}, spread over a size of 0.36”×0.25” without significant regularity, but notably lacking thermal radiation flux.

G90.925+1.486. This methanol maser source was discovered in 2000 by Szymczak et al. (2000). The BeSSeL survey determined a parallax of 0.171±0.031 mas for this object, corresponding to a distance of $5.9^{+1.3}_{-0.9}$ kpc (Reid et al., 2019). Using JVLA (Hu et al., 2016), the 6.7 GHz maser emission was detected in a broad region of approximately 0.4”×0.5”, ranging from -71.5 to -68.31 km s^{-1}. There is a notable velocity gradient from southwest to northeast. A radio thermal emission with an intensity of approximately 0.63 Jy was observed about 0.15” southeast of the maser position.

G94.602−1.796. Also known as V645 Cyg and AFGL2789, this object is an early evolutionary stage source with a central O7 spectral class star (Cohen, 1977) and optically significant gas outflow (Clarke et al., 2006). Its trigonometric parallax is measured to be 0.221±0.013 mas, corresponding to a distance of $4.5^{+0.3}_{-0.2}$ kpc (Reid et al., 2019). Val’tts et al. (2002) observed this source with the EVN in 1998 and 2000 using five telescopes. Their images reveal four groups of masers and indications of disk rotation. JVLA results (Hu et al., 2016) indicate maser emission ranging from -44.08 to -40.39 km s^{-1} VLSR, distributed in a size of 0.10”×0.22”, with a north-to-south velocity gradient, as well as radio thermal emission with an intensity of 0.42 Jy.

The application was submitted on June 1, 2019, and received a rating of 1.4 points from the EVN Program Committee (0 - high priority, 3 - lowest priority).

All the requested 10 hours were allocated on the available telescopes for the autumn 2019 session. These observations can be found in the EVN schedule and archive under program code EA063.

5.2 Observation

After securing the most suitable ten hours, in collaboration with JIVE support scientists, a detailed observation plan had to be established. For each source, a nearby (within 2 degrees) phase calibrator needed to be identified. The following calibrators were selected: J2007+4029 for G78.122+3.633, J2114+4953 for G90.925+1.486, and J2007+4029 for G94.602-1.796. In addition, 3C345, a bright quasar, was chosen for instrumental effects calibration.

JIVE (Joint Institute for VLBI ERIC), based in the town of Dwingeloo, the Netherlands, performed data correlation using the SFXC correlator (Keimpema et al., 2015). Typically, for line observations, the data is correlated twice: first, using all eight 4 MHz frequency bands (approximately 200 km s^{-1}) with 128 channels in each band to ensure a good signal-to-noise ratio for phase calibrators. The second time, only the band containing maser emissions is correlated, with 2048 channels, equivalent to 1.95 kHz per channel (0.088 km s^{-1}). As neither I nor colleagues at the institute had sufficient experience in processing VLBI data, we took the opportunity to visit JIVE and learn there. The duration of the knowledge acquisition mission was one week, after which the data was successfully processed and ready for interpretation. Data reduction follows the EVN guidelines, which are well-documented on their website[2].

Overall, the EA063 observation was successful, and there was little data that needed to be discarded. The effective on-source integration times were approximately 135, 105, and 98 minutes for the three sources. For data processing, Effelsberg was used as the reference antenna. The synthesized beam size was approximately 4 mas x 3 mas, with a position angle of -60 degrees. Data cubes with a size of 1024 px x 1024 px, corresponding to 1 mas per pixel, were generated. The image noise level was approximately 3.8 mJy $beam^{-1}$. Gaussian fitting for maser spot parameters was performed using the AIPS tool JMFIT, which effectively carries out two-dimensional Gaussian fitting.

5.3 Results

Using the EVN, high-resolution images of the three selected objects were obtained at milliarcsecond resolution. Images of G90.925+1.486 and G94.602−1.796 of such quality were obtained for the first time.

In the case of **G78.122+3.633**, we identified 98 maser spots grouped into 14 cloudlets in the image. These are defined as a group of maser spots with S/N>10,

[2]https://www.evlbi.org/evn-data-reduction-guide

occurring in at least three consecutive channels, and with angular separations not exceeding half of the synthesized beam size (Bartkiewicz et al., 2020). The parameters of the maser cloudlets are summarized in Table 5, which includes their relative coordinates (ΔRA, ΔDEC) relative to the maser spot with an LSR velocity of -4.9 km s^{-1} and position RA=$20^h14^m26.05839^s$, Dec=$+41^o13'32.5278''$ (J2000). In this case, we do not use the brightest maser spot as a reference, as it allows for easier comparison of the results with Moscadelli et al. (2011). The relationship between the radial velocity and intensity of the maser spots was modeled using a Gaussian function, allowing the determination of the following parameters: V_{fit} represents the radial velocity at which the flux of the function is highest (S_{fit}), and the line width (FWHM). The maximum linear size (L_{proj}) is the largest distance between two maser spots. If a regular decrease/increase in velocity was observed in the cloudlet structure, the velocity gradient (V_{grad}) was determined by dividing the difference in radial velocity by the linear distance. The sign of V_{grad} is disregarded. The orientation of this gradient is indicated by the position angle (PA), which is determined by the main axis of the cloudlet distribution, starting from the blue-shifted to red-shifted spots, with the positive direction being eastward. It should be noted that the linear regression takes into account the flux densities of the maser spots. The average FWHM value for all cloudlets is 0.31 ± 0.02 km s^{-1}. The obtained structures are best represented in the image in Figure 6 (left panel), and attention should also be paid to the upper panel, where the EVN and RT–16 spectra are compared, revealing that the measured flux density with EVN is about 57% lower. The maser emission was observed in a radial velocity range from -4.77 to -8.37 km s^{-1}, covering an area of approximately 300 mas $\times$ 160 mas in the sky, corresponding to approximately 480 AU $\times$ 260 AU. The individual cloudlets occupy emission areas ranging from 0.5 to 7 mas, with a mean L_{proj} of 4.2 ± 0.3 AU. The velocity gradient ranges from 0.05 to 0.45 km s^{-1} AU^{-1}, with an average value of 0.14 ± 0.03 km s AU^{-1}. Among all the parameters, only L_{proj} and S_{fit} show a moderately significant correlation (r=0.596).

In Figure 7, we present a map of the cloudlets showing their velocity gradient directions, noting that negative PA values are inverted in the 0 – 180°range. Cloudlets with relatively high (above 0.14 km s^{-1} AU^{-1}) velocity gradient values are predominantly located in the central region of the source, and their orientations are approximately orthogonal to the plane of the protoplanetary disk. However, the overall distribution of cloudlet PAs does not follow this trend, especially for cloudlets with low gradient values, as their PA values span a wide range. This could indicate the presence of complex gas kinematics within structures of 5 – 20 AU in size. The direction of the velocity gradient for maser cloudlet number 5 aligns with the direction of the peculiar motion vector (Moscadelli et al., 2011), suggesting that this cloudlet moves together with an outflowing gas.

For the source **G90.925+1.486**, the maser emission is shown in Figures 6

Table 5: Parameters of the 6.7 GHz methanol maser cloudlets in G78. ΔRA and ΔDec correspond to the relative coordinates to the maser spot at RA=$20^h14^m26.05839^s$, Dec=+$41^o13'32.5278''$ (J2000). V_p is the peak velocity, V_{fit} is the fitted velocity, FWHM is the full-width at half maximum of the Gaussian profile, S_p is the peak brightness, S_{fit} is the fitted brightness, L_{proj} is the projected linear size of cloudlet, V_{grad} is the velocity gradient and PA is the position angle of the major axis of cloudlet. Entries in italic are uncertain.

Cloudlet	ΔRA (mas)	ΔDec (mas)	V_{fit} (km s^{-1})	FWHM (km s^{-1})	S_{fit} (Jy beam^{-1})	L_{proj} (mas(AU))	V_{grad} (km s^{-1} mas^{-1}(km s^{-1} AU^{-1}))	PA (°)
1	0.0	0.0	-4.94	0.26	0.12	1.3(2.1)	0.29(0.173)	*51*
2	83.2	106.2	-6.93	0.33	1.38	5.5(8.8)	0.13(0.079)	122
3	54.1	112.1	-6.85	*0.76*	0.11	6.8(10.9)	0.10(0.064)	-65
4	33.9	139.9	-7.60	0.27	0.42	0.6(1.0)	0.72(0.451)	119
5	-168.9	104.6	-6.72	0.31	0.80	1.1(1.7)	0.14(0.085)	108
	-158.1	101.7	-6.08	0.41	8.09	6.9(11.1)	0.14(0.085)	92
6	-96.5	94.1	-6.60	0.24	0.22	1.6(2.6)	0.11(0.067)	139
	-100.4	80.6	-5.69	0.40	0.68	2.7(4.3)	0.20(0.123)	-114
7	122.1	106.0	-8.27	0.29	0.45	4.2(6.7)	0.13(0.079)	-137
8	107.2	106.5	-7.75	0.31	0.04	2.4(3.8)	0.07(0.046)	-107
9	-74.2	91.7	-6.71	0.36	0.37	0.6(1.0)	0.56(0.352)	*-30*
10	47.0	109.8	-7.10	0.25	0.51	1.2(1.9)	0.23(0.142)	-44
11	-94.6	86.2	-6.41	0.37	0.58	2.5(4.0)	0.17(0.109)	-133
12	-67.5	92.0	-6.70	0.33	0.17	1.4(2.2)	0.12(0.076)	45
13	-88.7	95.8	-	-	-	0.8(1.3)	0.22(0.136)	*-31*
14	-94.9	-80.9	-5.86	0.46	0.41	3.3(5.3)	0.11(0.066)	-67

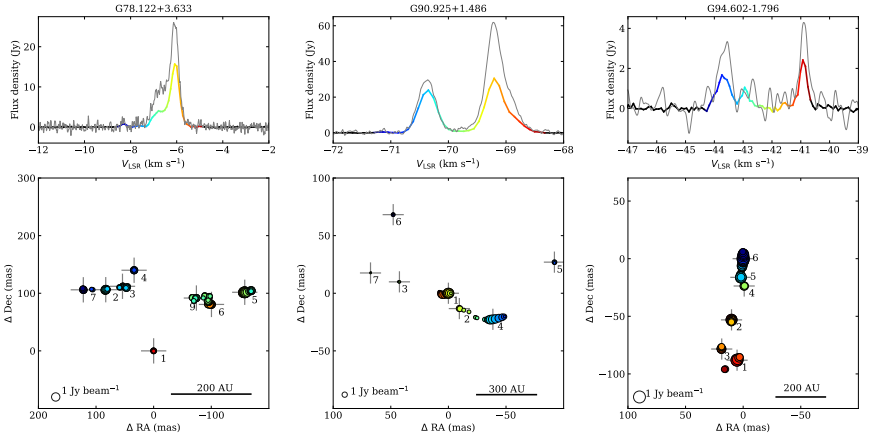

Figure 6: Top: Maser spectra of G78, G90 and G94 as obtained by EVN (colour) and the Irbene 16m radio telescope (grey line) on 31 October 2019. Bottom: Distribution of methanol maser spots. The colours are related to the LSR velocity as in the spectrum. The spot size is proportional to the logarithm of its brightness. The cloudlets (crosses) are numbered as listed in Tables 5, 6 and 7.

Table 6: The same as Table 5 but for G90.925+1.486. Coordinates of the (0,0) point are RA=$21^h09^m12.97474^s$, Dec=$+50^o01'03.6580$" (J2000) and corresponds to the brightest maser spot.

Cloudlet	ΔRA	ΔDec	$V_{\rm fit}$	FWHM	$S_{\rm fit}$	$L_{\rm proj}$	$V_{\rm grad}$	PA
	(mas)	(mas)	(km s^{-1})	(km s^{-1})	(Jy beam^{-1})	(mas(AU))	(km s^{-1} mas^{-1} (km s^{-1} AU^{-1}))	(°)
1	0.0	0.0	-69.21	0.30	21.71	2.8(12.4)	0.18(0.031)	93
	5.1	-1.4	-68.79	0.24	3.10	4.3(19.5)	0.14(0.024)	62
2	-9.5	-13.3	-69.41	0.28	1.64	0.6(3.3)	0.35(0.060)	68
	-14.1	-7.7	-69.82	0.24	0.38	1.9(11.5)	0.10(0.018)	62
3	42.5	9.9	-69.59	0.36	0.19	1.1(6.4)	0.18(0.031)	*-96*
4	-38.6	-22.6	-70.34	0.34	9.37	17.5(103.2)	0.05(0.008)	100
5	-92.0	27.0	-70.49	0.32	0.65	0.7(4.0)	0.29(0.050)	6
6	47.9	68.2	-71.14	0.19	0.40	0.9(5.4)	0.32(0.055)	*143*
7	67.6	17.6	-69.60	0.34	0.10	1.0(5.7)	0.20(0.035)	*146*

Table 7: The same as Table 5 but for G94.602−1.796. Coordinates of the (0,0) point are: RA=$21^h39^m58.25561^s$, Dec=$+50^o14'20.9108$" (J2000) and corresponds to the brightest maser spot.

Cloudlet	ΔRA	ΔDec	$V_{\rm fit}$	FWHM	$S_{\rm fit}$	$L_{\rm proj}$	$V_{\rm grad}$	PA
	(mas)	(mas)	(km s^{-1})	(km s^{-1})	(Jy beam^{-1})	(mas(AU))	(km s^{-1} mas^{-1} (km s^{-1} AU^{-1}))	(°)
1	5.3	-88.1	-40.85	*0.53*	1.05	5.1(23.0)	0.11(0.024)	137
2	10.1	-53.1	-40.98	0.30	0.59	2.3(10.4)	0.36(0.081)	-30
	10.1	-53.7	-41.43	*0.58*	0.10	2.6(12.0)	0.42(0.091)	-21
3	18.6	-78.4	-41.07	*0.56*	0.15	2.1(9.5)	0.23(0.051)	179
4	-0.9	-23.7	-42.20	0.19	0.12	0.5(2.3)	0.43(0.96)	*85*
5	2.0	-16.2	-42.94	0.36	0.54	5.7(25.7)	0.14(0.031)	3
6	0.0	0.0	-43.65	*0.54*	0.96	14.0(63.0)	0.11(0.024)	7

(center). We identified 47 methanol maser spots grouped into seven different cloudlets, and their parameters are listed in Table 6. The average linewidth (FWHM) of individual lines is 0.30 km s^{-1}. The emission was detected in the radial velocity range from −71.31 to −68.31 km s^{-1}. It covers an area of 160 mas × 90 mas, corresponding to approximately 950 AU×530 AU. The linear sizes of the cloudlets range from 6 to 100 AU. The lower–blue-shifted component shows a significant velocity gradient with a total value of 0.007 km s^{-1}AU^{-1}. Overall, the velocity gradient directions of the cloudlets align with the overall elongation of the structure. Comparing the EVN spectrum with our telescope, it is evident that the component with an LSR velocity of −69.2 km s^{-1} is well resolved by 63%, while the −70.3 km s^{-1} component is only resolved by 19%. The overall integrated brightness ratio S_{int}(EVN)/S_{int}(Ir) is 0.43.

The source **G94.602−1.796** is the weakest source which we observed and is shown in Figures 6 (right). The maser emission originated from 59 spots distributed among six cloudlets, and their parameters are listed in Table 7, covering −40.55 to −44.4 km s^{-1} LSR range. The emission covers a elongated region oriented north–south, with dimensions of 33 mas×115 mas, corresponding to approximately 150 AU×520 AU in physical size. It exhibits a noticeable velocity gradient of 0.035 km s^{-1} mas^{-1} (0.008 km s^{-1} AU^{-1}). The integrated brightness ratio S_{int}(EVN)/S_{int}(Ir) in the spectrum is 0.42, and the average FWHM of the components is 0.37 km s^{-1}.

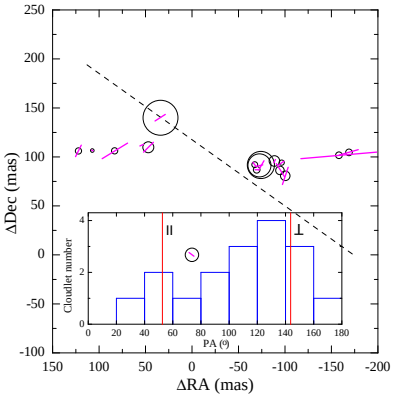

Figure 7: Map of velocity gradient directions (magenta bars) for the maser cloudlets in G78 from the 2019 EVN data. The length of the bars is proportional to the square of brightness, and the circle size is proportional to the velocity gradient. The diagonal black dashed line marks the direction of the disc plane (Cesaroni et al., 2005). The inset shows the position angle (PA) histogram of the velocity gradient; the two vertical red lines mark directions parallel and orthogonal to the plane of the disc.

5.4 Analysis and discussion

When comparing the spectra obtained with the interferometer to those obtained with an individual telescope, it is evident that the EVN significantly resolves them, with a flux loss of 57-58%. This flux loss is not dependent on the source brightness or distance. Similar flux loss density was reported by Bartkiewicz et al. (2016) when examining a large number of sources. It should be noted that the spectral components of G90.925+1.486 are resolved to varying degrees.

5.4.1 G78.122+3.633

We also conducted a study on the individual structure evolution of maser features with sub-arcsecond precision. G78.122+3.633 was observed with the EVN in 2004, 2007, 2009, and 2011 (program codes EL032, EM064C, EM064D, and ES066E). We downloaded and processed the archival data similar to our own. Except for the 2011 data, the radial velocity resolution is the same, but for this observation, it is twice as high, at 0.044 km s^{-1}. The overall distribution of maser features in G78.122+3.633 over five different epochs, spanning 15 years, is shown in Figure 12. We found that seven maser features are present in all five EVN observations, and their parameters are listed in Table 8. By studying the distribution of maser features using the weighted least squares method, we fit a straight line that characterizes their major axis. The linear correlation coeffi-

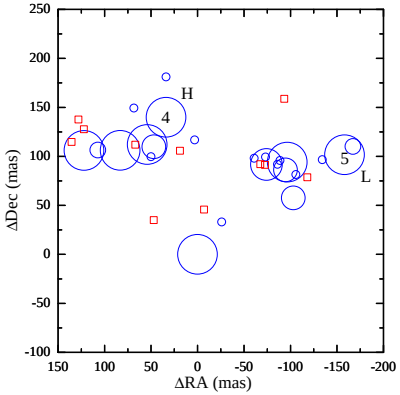

Figure 8: Map of maser cloudlets detected with five epoch EVN observations in 2004-2019 interval in G78.122+3.633. The symbol size is proportional to the number of epochs in which the cloudlet appeared. The blue circles and red squares mark the cloudlets with and without Gaussian profiles, respectively. Cloudlets 4 and 5 (Table 5) identified with the spectral features showing the highest and lowest variability evaluated from χ^2_r (Table 5) are labelled with H and L, respectively.

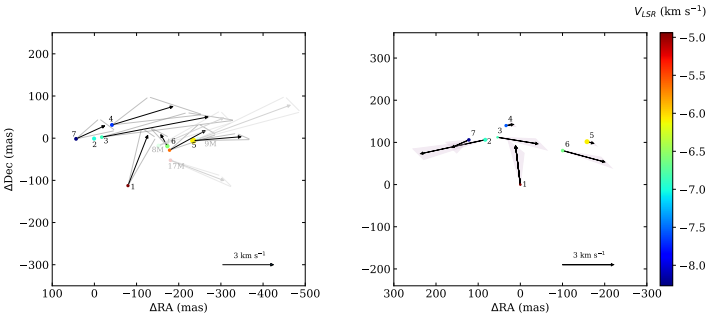

Figure 9: Relative proper motions of 6.7 GHz maser cloudlets in G78.122+3.633. **Left:** Results for the model of the disk-jet interface scenario by Moscadelli et al. (2011) over a period of 2004-2019. The numbers correspond to the names of persistent cloudlets as given in Table 8. The light-coloured circles and light grey vectors correspond to features 8, 9, and 17 from Table 1 in Moscadelli et al. (2011); they were not detected in 2011 and 2019. The grey triangles correspond to the uncertainties of proper motion vectors. **Right:** Relative proper motions derived from distance changes between cloudlet pairs.

cient r_s was calculated based on the alignment of maser feature (mathematically treated as points) distribution with the fitted line. Similarly, the correlation coefficient r_v was determined, which describes the radial velocity variation of maser features as a function of their distance from the major axis. An example of this information is shown in Figure 13. Feature 1 (Figure 13) is the most compact in all five observations, resulting in poorly determined parameters (r_s, r_v, $V_{\rm grad}$, and PA). The brightest features of the second feature form a linear structure with high values of r_s, r_v, and nearly constant $\pm 10°$PA. The structure of the third feature has changed significantly from three compact features in 2004 to a complex structure with two maxima starting in 2009. The fourth feature is very compact. The highest radial velocity features in the fifth feature form a uniquely curved structure that remains stable for 15 years. A lower velocity component appeared in 2009 and has a consistently linear structure in the last two observations. This feature is the closest to the outflow where active 22 GHz water masers are present (Moscadelli et al., 2011), and its velocity gradient direction is very close to the gas flow direction. It should be noted that the brightness variation of this feature differs significantly from the others, with its peak occurring in 2009. This suggests that the density variations in this feature are less dependent on changes in the protostar's activity. The sixth feature is significantly twisted, and its morphology is highly variable. The morphology of the seventh feature is arc-like, and we observed gradual straightening. In conclusion, the structure and brightness of the seven stable features exhibit significant variations over a period of 2 to 15 years.

In addition to the seven persistent maser features, we also detected 27 transient features, with 21 of them observed only in a single EVN epoch. Eleven of them did not exhibit a Gaussian profile, possibly because VLBI detects only the most compact emission region with low maser amplification levels. Figure 8 shows the distribution of these features, with the symbol size indicating the number of epochs in which a particular feature was observed. Interestingly, the transient features are located to the north of the persistent features, but almost never to the south. Features 4 and 5 correspond to the main flux sources of the most variable and less variable spectral component, indicated by H and L in the plot. The position of the 6.7 GHz methanol maser partially coincides with the emission zone of CH_3CN (J = 12−11, K=3), which has an excitation temperature of 133 K. Further to the south, higher-energy CH_3CN emissions appear (see their Fig. 5; Cesaroni et al., 2014). This suggests that the regions where methanol emission is not observed have a higher kinetic temperature, according to the standard model for methanol maser excitation (Cragg et al., 2002).

The results of the five-year monitoring campaign in Irbene are similar to those obtained by Szymczak et al. (2017) from 2009 to 2013. The -7.7 km s^{-1} component shows significant variability, while the -6.1 km s^{-1} component is less variable. Examining the spectrum of the 6.7 GHz maser in earlier observations of this source indicates that G78.122+3.633 has been actively changing for at least

the past 27 years.

Using all five available EVN observation data, we performed a proper motion analysis of the target source. We initially followed the same approach as Moscadelli et al. (2011), with the second maser feature at an LSR velocity of -7.1 km s^{-1} serving as the reference point. The procedure was as follows: (1) identify features observed in all five EVN epochs, (2) check if these features exhibit linear motion relative to the second feature, (3) finally, estimate the linear motion magnitude using linear regression with all five observation data points. The direction and speed of proper motion are shown on the left in Figure 9. Overall, our results closely resemble those obtained by Moscadelli et al. (2011) when they estimated the motion over five years using three data sets. The motion speeds range from 1.5 to 6.0 km s^{-1}, and the positional angle (PA) difference from the direction of the proper motion vector is less than 30 degrees. In the eastern cluster of features, we observed another feature that can undergo proper motion estimation, while three features that were analyzed for proper motion by Moscadelli et al. (2011) disappeared in later observations. The internal motion estimation supports the hypothesis that the western cluster of features follows the gas motion rising from the disk near the outflow starting point, as indicated by the 22 GHz water masers (Moscadelli et al., 2011). Additionally, we applied a different approach to estimate the proper motion. The procedure involved: (1) measuring the distances between all pairs of the seven stable features (a total of 21 pairs), assuming the position of the first feature as (0,0), (2) fitting lines using the least squares method that describe uniform motion for each pair (resulting in six vectors for each feature), (3) calculating the summed vectors for each feature, which represents its motion. The result of this method is shown on the right in Figure 9. The first feature moves towards all the others, similar to the first method. The second and seventh features move away from the third and fourth, as well as from the features located further west. The features located furthest to the north (features 4, 5, and 7) exhibit very low motion speeds (below 1 km s^{-1}), which significantly differs from the speed values of other features closer to the central star, approximately 400 AU to the south (Cesaroni et al., 2013). Therefore, the results of this method do not agree with the postulated model of the disk and disk-jet interaction zone (Moscadelli et al., 2011), but they could correspond to the spatially turbulent disk kinematics directly observed in CH_3CN emission line maps (Cesaroni et al., 2014).

5.4.2 G90.925+1.486

The overall structure is very similar to what was obtained by the BeSSeL survey using the VLBA in 2012. Cloudlets 1, 2, 4, and 6 have matching LSR velocities and positions with the BeSSeL data. The remaining two features were not detected in 2012, most likely due to the higher resolution of the VLBA. JVLA observations in 2012 (Hu et al., 2016) revealed an extended

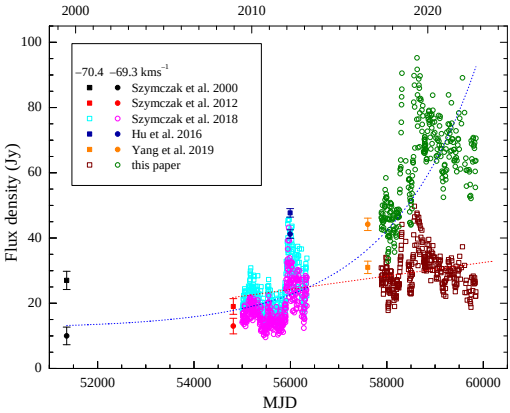

Figure 10: Long term variations of the peak flux density of the −70.4 and −69.3 km s^{-1} features in G90 marked as squares and circles, respectively. The flux calibration accuracy is ∼10 per cent for the MJD 55005-56340 data and ∼20 per cent after MJD 57885. The red and blue dotted lines mark the best fits of linear (r=0.46, p<0.001) and exponential (r=0.80, p<0.001) curves to the −70.3 and −69.3 km s^{-1} time series, respectively.

∼300×600 mas (∼1700×3500 AU) emission region, indicating an expanded region of emission amplification distinguishable by the VLBA and EVN. The emission from feature 4 at -70.3 km s^{-1} maintained its morphology for 7 years. Other features underwent more significant changes, but their PA variations remained within 40 degrees. Overall, the morphology remained stable for 7 years.

VLBI data and monitoring results indicate that the spectral component with an LSR velocity of -69.2 km s^{-1} originates from the first feature, while the less variable component at -70.3 km s^{-1} comes from the fourth feature. Monitoring results show that over the past 4 years, with cycles lasting 2 to 3 months, these components have changed synchronously with amplitudes ranging from 20% to 50%. Comparing these observations with the 2009-2013 period (Szymczak et al., 2017) reveals a similar behavior of these components. By combining all available G90.925+1.486 spectrum data from the literature (Szymczak et al. 2000, 2012; Szymczak et al. 2017; Hu et al. 2016; Yang et al. 2019) and our monitoring results, it is evident that the ratio between the peak fluxes of the -70.4 and -69.2 km s^{-1} components monotonically decreases from 2.5 to 0.4 over the period from 1999 to 2022 (see Figure 10). Since 6.7 GHz methanol maser emission is stimulated emission (Cragg et al., 2002), synchronous fluctuations on timescales ranging from 3 months to several years, with amplitude fluctuations of up to a factor of 3.8, indicate significant changes in the pumping radiation intensity from the central object. Figure 10 shows that the flux of the -70.4 km s^{-1} component increases

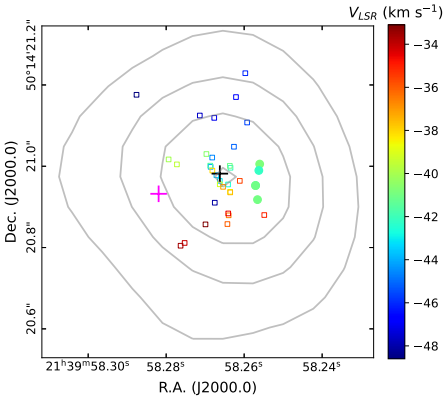

Figure 11: Map of the 1.37 mm continuum in G94 (Beuther et al., 2018). The first contour is at 4.0 mJy beam^{-1} with steps increasing by 2.0 mJy beam^{-1}. It is overlayed with the 6.7 GHz maser cloudlets (filled circles) and the peaks of the CH_3CN 220747.261 GHz line emission (open squares) retrieved from the NOEOMA data (Gieser et al., 2021). The colour indicates the LSR velocity according to the scale shown in the wedge. The black and magenta crosses mark the peak of continuum emission at 5.8 and 44 GHz, respectively (Purser et al., 2021).

very slowly (0.75 Jy yr^{-1}) from 2008 to 2022, while the flux of the -69.2 km s^{-1} component increases exponentially (7-fold in 23 years). The author hypothesizes that the observed fluctuations in flux density are caused by changes in the active environment's size (length) resulting from gas motion (Caswell et al. 1995) and spiral arms in the disk (Bayandina et al. 2022).

5.4.3 G94.602-1.796

The spectrum of this source has significantly changed compared to the data from the Irbene Observatory, as found in the literature (Szymczak et al. 2017; Hu et al. 2016). The emission with a radial velocity of -43.2 to -42.2 km s^{-1} has decreased by a factor of two. Examining even older data (Slysh et al. 1999; Szymczak et al. 2000), significant differences in the spectral structure can be observed.

VLBA data was obtained as part of the BeSSeL program during observations in December 2012. During these observations, 12 maser spots were identified, most likely corresponding to cloudlets 1, 2, 4, 5, and 6. Due to the spectral resolution of only 0.36 km s^{-1}, it was not possible to analyze the structure of the cloudlets, but it should be noted that the overall morphology of the source, with a vertical linear structure and a velocity gradient, is very similar. Comparing the positions of the maser features with the highest amplitudes, which had nearly identical radial velocities in 2012 and 2019, there is no significant motion ob-

served (0.85 mas). Lower spatial resolution observations with VLA-C (Hu et al. 2016) and EVN (Slysh et al. 2002) also show similar spatial morphology, suggesting that the overall structural properties have remained stable for at least 20 years, with observed changes likely associated with individual cloudlet variations (Szymczak et al. 2017).

Near-infrared observations of G94.602−1.796 revealed that the outflow is oriented almost towards the observer (Murakawa et al., 2013). On the other hand, compact thermal emission detected at 5.8 and 44 GHz with intensities of approximately 0.23 and 0.52 mJy, respectively, exhibits an elongation position angle of 91±71°, suggesting a candidate for the source of the outflow (Purser et al., 2021). It is important to note that the peak of the thermal emission in the C-band is only 100 mas away from the position of the masers. This region of the sky was also observed at 1.3 mm, where four sources were detected. The strongest source is located approximately 90 mas away from the position of the methanol masers. Spectral data from the NOEMA survey (Gieser et al., 2021) provided us with a map of the 220747.261 GHz CH_3CN emission line, which is considered a good indication of molecular disks (Cesaroni et al. 2014). These thermal emission features, similar to the methanol maser spots, are oriented in a North-South direction with a clear velocity gradient (Figure 11). This suggests that the methanol masers are located in the central part of the western edge of the disk.

5.5 Conclusions

We compiled 4.5-year-long time series monitoring data for three sources and analyzed them in the context of VLBI data. The variations in source flux density are diverse, but their common feature is that all spectral components change synchronously. We successfully obtained arc-millisecond resolution images for three selected variable sources. For G90.925+1.486 and G94.602−1.796, data of this quality were obtained for the first time. When examining individual maser cloudlets, structural changes over time can be very significant, indicating rotation, contraction, or elongation, as well as their movement within the disk.

G78.122+3.633 has been an actively variable source for at least the last 27 years. Seven persistent maser cloudlets significantly change their velocity and flux over a few years. The cloudlets associated with the disk change considerably on both daily to monthly scales and over a longer 2 to 15-year period compared to the maser cloudlets located at the outer edge of the flux. We observed that the direction of most cloudlet velocity gradients aligns well with the direction of the cloudlet motion vector we determined using five datasets. Significant variations and a large number of temporarily appearing cloudlets indicate the unsaturation of maser emission in the disk zone.

In general, the structure of G90.925+1.486 has been stable for 7 years. The variability profile of the two main components is significantly different over 23

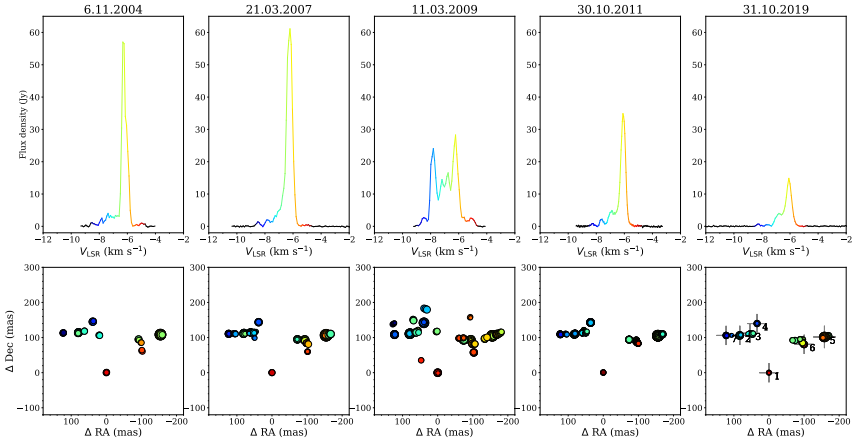

Figure 12: *Top:* The 6.7 GHz methanol maser spectra of G78.122+3.633 at five EVN epochs that were retrieved from the EVN Archive (projects EL032, EM064C, EM064D and ES066E) and our own. *Bottom:* Distributions of the methanol maser spots. The circle size represents the logarithm of its flux density and the colour corresponds to the LSR velocity as in the top panel. Coordinate centre (0,0) is the position of the spot at the LSR velocity of -4.9 km s^{-1} that was compact and stable in all epochs. Its coordinates are given in Table 5. Grey crosses and numbers on the most right panel mark positions of seven cloudlets that persisted over 15 yr.

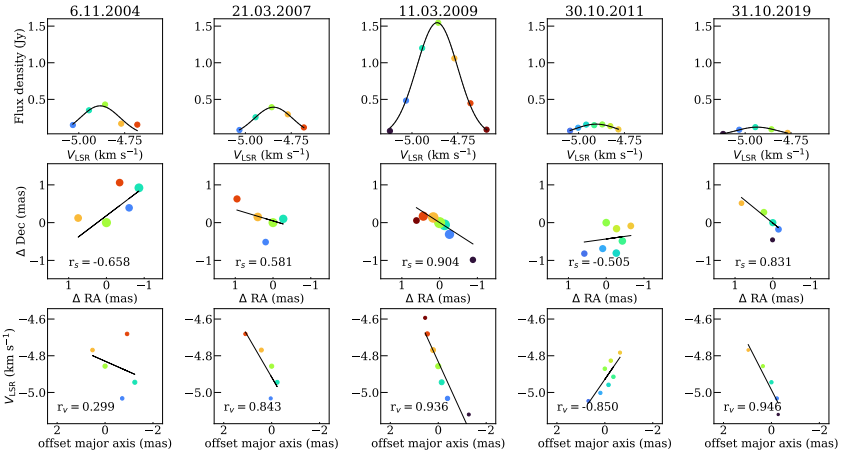

Figure 13: *Top:* Spectra of Cloudlet 1 as in Table 12 with a Gaussian velocity profile for five epochs. *Middle:* The spot distribution with the major-axis fit. A circle size is proportional to the logarithm of spot's flux density. The (0,0) point corresponds to spot position with max flux density at given epoch. *Bottom:* The spot LSR velocity vs position offset along the major axes. The correlation coefficients r_s, r_v are listed.

Table 8: Parameters of the 6.7 GHz maser cloudlets in G78.122+3.633 that persisted 15 years. The parameters are the same as in Table 5 but for all five epochs. We also list the correlation coefficients of maser spot distribution (r_s) and offset of major axes (r_v) and the position angle of the major axis of maser spots with each cloudlet (PA).

Cloud	ΔRA	ΔDec	$V_{\rm fit}$	FWHM	$S_{\rm fit}$	r_s	r_v	$V_{\rm grad}$	PA
Epoch	(mas)	(mas)	(km s^{-1})	(km s^{-1})	(Jy beam^{-1})			(km s^{-1} mas^{-1}(AU)$^{-1}$)	(°)
Cloudlet 1									
2004	0.0	0.0	-4.88	0.26	0.4	-0.66	0.36	0.20(0.12)	*127*
2007	0.0	0.0	-4.85	0.25	0.4	0.58	0.88	0.26(0.16)	*73*
2009	-0.2	-0.1	-4.86	0.26	1.5	0.90	0.93	0.29(0.18)	*57*
2011	0.3	0.8	-4.90	0.27	0.2	-0.51	-0.92	0.18(0.12)	*-82*
2019	0.0	0.0	-4.94	0.26	0.1	0.83	0.95	0.28(0.17)	*51*
Cloudlet 2									
2004	79.3	114.4	-7.15	0.17	1.9	-0.90	0.94	0.28(0.18)	142
2007	79.7	112.4	-7.14	*0.52*	1.7	-0.89	0.77	0.13(0.08)	134
2009	78.6	111.2	-7.10	0.42	9.2	-0.65	0.59	0.15(0.09)	129
2011	82.3	109.4	-6.93	0.20	1.2	-0.99	0.99	0.12(0.07)	123
	-	-	-7.07	*0.47*	1.0	-	-	-	-
2019	83.2	106.2	-6.93	0.33	1.4	-0.99	0.99	0.13(0.08)	122
Cloudlet 3									
2004	62.4	118.0	-	-	-	-0.99	-0.90	0.26(0.16)	*-29*
2007	62.2	114.5	-7.00	0.43	0.9	-0.72	-0.79	0.08(0.05)	*-100*
2009	61.6	114.9	-6.94	0.26	1.4	-0.54	0.24	0.04(0.03)	88
	56.3	120.0	-6.56	0.23	0.5	-0.94	-0.99	0.07(0.05)	-31
2011	60.1	113.3	-7.00	0.41	0.4	-0.90	-0.90	0.19(0.12)	-53
	55.8	121.5	-6.49	0.26	0.1	-0.91	-0.97	0.04(0.03)	-26
2019	54.1	112.1	-6.85	*0.76*	0.1	-0.94	-0.98	0.10(0.06)	-65
Cloudlet 4									
2004	38.3	145.6	-7.67	0.29	1.1	-0.59	0.94	0.10(0.06)	*109*
2007	38.1	143.7	-7.64	0.29	1.1	-0.67	0.82	0.10(0.06)	*99*
2009	38.8	142.2	-7.73	*0.28*	9.2	-0.10	-0.21	0.19(0.12)	*101*
2011	36.3	142.9	-7.62	0.27	1.8	0.91	-0.98	0.48(0.30)	153
2019	33.9	139.9	-7.60	0.27	0.4	-0.72	0.95	0.72(0.45)	119
Cloudlet 5									
2004	-154.2	108.4	-6.10	0.33	27.8	0.80	0.97	0.11(0.07)	79
2007	-154.3	106.6	-6.09	0.36	60.7	-*	0.97	0.12(0.07)	76
2009	-168.8	109.3	-6.74	0.32	2.2	-0.99	0.95	0.10(0.06)	118
	-155.6	105.0	-6.08	0.39	23.7	-*	0.92	0.11(0.07)	77
2011	-168.9	109.4	-6.76	0.35	0.9	-0.99	0.75	0.09(0.05)	115
	-155.9	105.1	-6.08	0.38	26.4	0.46	0.78	0.11(0.07)	75
2019	-168.9	104.6	-6.71	0.31	0.8	-0.56	0.65	0.14(0.09)	108
	-158.1	101.7	-6.08	0.41	8.3	-0.81	0.99	0.14(0.09)	92
Cloudlet 6									
2004	-91.7	95.3	-6.64	0.32	0.6	0.38	-0.73	0.37(0.23)	*97*
	-98.5	85.5	-	-	-	-	-	-	-
2007	-93.8	93.4	-6.52	0.33	2.9	0.62	0.99	0.11(0.07)	-128
	-98.1	83.8	-5.49	0.45	0.5	0.67	0.79	0.28(0.18)	70
2009	-94.7	93.4	-6.52	0.30	4.2	0.87	-0.98	0.09(0.06)	-162
	-99.0	82.2	-5.50	0.48	1.2	-0.88	-0.97	0.27(0.17)	-72
2011	-93.4	89.8	-6.39	0.44	0.3	0.71	-0.99	0.09(0.06)	-138
	-99.0	83.1	-5.74	*0.82*	0.4	0.91	-0.95	0.14(0.08)	-112
2019	-96.5	94.1	-6.60	0.24	0.2	0.79	-0.94	0.11(0.07)	139
	-100.4	80.6	-5.70	0.40	0.7	0.70	-0.80	0.20(0.12)	-114
Cloudlet 7									
2004	123.1	113.0	-8.34	0.34	0.5	-0.96	0.41	0.17(0.11)	*127*
2007	123.2	110.5	-8.30	0.32	1.0	0.52	-0.95	0.30(0.19)	-147
2009	122.9	108.5	-8.30	0.32	2.1	0.33	-0.98	0.26(0.16)	-132
2011	122.5	109.0	-8.27	0.30	0.6	0.85	-0.99	0.15(0.09)	-140
2019	122.1	106.0	-8.27	0.29	0.5	0.87	-0.98	0.13(0.08)	-137

*The correlation coefficient is undefined because the EW spot distribution, i.e. variance of Y is zero.

years; one changes linearly with a rate of $0.75\,\mathrm{Jy\,yr^{-1}}$, while the other's flux increases exponentially. The most likely reason for these variations is changes in the length of the active environment.

The structure of G94.602−1.796 has also been generally stable for at least 7 years. The radiation of the main components comes from different cloudlets, and their brightness varies from 0.5 to 5.82 times, in the shortest time period (up to 3 months), the components fluctuate synchronously with a relative amplitude of 1.0 to 1.5. Short-term variability is mainly caused by changes in the pumping radiation intensity, while long-term changes are related to gas motion.

5.6 Author contribution

As mentioned earlier, before this study, the institute had limited experience in conducting VLBI observations, data processing, and analysis. Knowledge transfer from colleagues in Toruń played a crucial role in the execution of this study, especially from Anna Bartkiewicz, who provided consultation at all stages of the research, and Marian Szymczak, with whom discussions regarding result interpretation were held. Some elements of data processing scripts were adopted from their students, Agnieszka Kobak and Michał Durjasz. Various data visualization tools were programmed with the assistance of Jānis Šteinbergs. As indicated in the data processing section, JIVE support scientists and staff undertake specific measures to make the observation process smoother and more successful for applicants.

The author prepared the proposal for the EVN observation and served as the Principal Investigator (PI). A detailed observation plan was developed. After data correlation, a visit to JIVE was made to learn the process of EVN data reduction and to process the obtained observational data. The author also familiarized themselves with the literature relevant to the research. Data visualization and measurements of statistical parameters and calculations were carried out. Additionally, archival data related to maser cloudlet evolution studies were processed. The obtained results were summarized and interpreted and subsequently published in the MNRAS journal, with the author being the first and corresponding author of this publication.

6 Closing remarks

6.1 Conclusions

The radio telescopes at the Ventspils International Radio Astronomy Center in Irbene have been successfully adapted for maser line observations. The introduced methodology complies with international standards. Technical solutions employ cutting-edge technologies such as SDR (Software-Defined Radio) and the latest publicly available software for astronomy.

Using both telescopes, it has been possible to obtain five-year-long time series of maser flux density. Most observations have been carried out with RT-16, as RT-32 continued to undergo modernization. The assessment of amplitude precision indicates a relative error of about 20%. This can be explained by the telescopes' proximity to the sea and very high humidity during the winter months. We have observed significant changes in the variability trends of several sources, including possible periodic fluctuations in three sources.

In this work, one of the first EVN observations, with the principal investigator (PI) being a scientist from Latvia, was carried out. It resulted in obtaining the first milliarcsecond-resolution images of two maser sources. The results for G90.925+1.486 reveal two components with significantly different resolved flux densities. Long-term monitoring indicates distinct trends, with one component's brightness increasing linearly and the other exponentially. However, in the shorter time period, both spectral components exhibit strongly correlated variations.

The image of G94.602−1.796 shows a prominently elongated structure extending from north to south. Several maser cloudlets are also stretched in the same direction. Based on these results, there is a high probability that we are observing a maser ring, oriented almost edge-on to Earth. Future observations, both those already conducted and repeat observations, will allow for the study of the evolution of individual cloudlets and a detailed analysis of both sources.

Analyzing a total of five G78.122+3.633 EVN observations, we concluded that the observed maser variability is primarily associated with changes in flux within maser cloudlets rather than the appearance or disappearance of new cloudlets. The evolution of individual cloudlets suggests their twisting, contracting, and stretching. There are indications that higher flux from the cloudlets is related to more pronounced and rapid morphological changes.

The variability and distribution of maser cloudlets in G78.122+3.633 are closely linked. The first group of cloudlets, located above the disk and falling onto it, exhibits significantly higher variability both in the short term (months) and long term (years) compared to the second group of cloudlets located at the disk and material outflow boundary. Comparing the individual morphology of cloudlets in both groups, we find that the cloudlets in the second group are larger and more concentrated. The recent rapid changes, observed only in the spectral

component corresponding to the first group of cloudlets, along with the relatively subtle changes in the second group, indicate that the cloudlets in the first group are unsaturated.

Analyzing the obtained changes in maser flux over five years, along with their images and results from previous studies, we conclude that the dominant variability observed in the sources is associated with changes in the activity of individual or multiple maser cloudlets. This suggests that changes in the intensity of pumping infrared radiation underlie the observed variability. Over a longer term, approximately 20 years, the motion of gas and system rotation also start to play a significant role.

6.2 Thesis

The introduced methodology for conducting maser observations allowed us to carry out the monitoring of 42 sources and validate the observations of the selected sources with the EVN.

- The radiotelescopes in Irbene are adapted for maser observations.
- The observed maser variability is primarily associated with changes in the intensity of existing maser cloudlets rather than their emergence or disappearance.

6.3 Conclusion

The thesis covers a broad scientific topic, specifically the activity of methanol masers in regions of massive star formation. Additionally, significant methodological and technical solutions have been achieved on a national scale for the application of VSRC telescopes in maser observations. The results presented in the thesis are novel and contribute to the field. The breadth of the topic presented in the doctoral thesis can be explained by the relatively short history of this research direction at VSRC. Establishing a local system that enables the acquisition of high-quality results was necessary to compete for the use of world-class instruments and engage in international collaboration. This has also been accomplished as part of this work. The quality of data from the Irbene radiotelescope is acceptable. However, challenges have arisen due to the telescopes' proximity to the sea and high humidity, which significantly reduces amplitude calibration precision. Additional calibration procedures and instrumental improvements are still in the development stage. The obtained time series of maser flux variability have relatively long observation intervals and provide valuable insights into changes in 42 individual sources over five years. Participation in the Maser Monitoring Organization (M2O) has opened up opportunities to engage in broader studies, with a focus on the most significant accretion events. Our aim is to continue and expand the maser monitoring program. The high-resolution images of two sources

obtained in the thesis provide significant insight into the nature of these systems, which certainly forms the basis for further investigation. Repeated observations are planned to determine the proper motion of maser spots and the global and individual cloudlet structural evolution. The results obtained have made a significant contribution to the study of G78.122+3.633.

References

Aller, M. F., Aller, H. D., and Hughes, P. A.: 2003, *The Astrophysical Journal* **586(1)**, 33–51

Antyufeyev, O., Bleiders, M., Patoka, D., Bezrukovs, V., Aberfelds, A., Shmeld, I., Orbidans, A., Steinbergs, J., Karelin, Y., and Shulga, V.: 2022, *Astronomical and Astrophysical Transactions* **33(2)**, 113

Araya, E. D., Hofner, P., Goss, W. M., Kurtz, S., Richards, A. M. S., Linz, H., Olmi, L., and Sewiło, M.: 2010, *The Astrophysical Journal Letters* **717(2)**, L133

Bally, J. and Zinnecker, H.: 2005, *The Astronomical Journal* **129(5)**, 2281

Bartkiewicz, A., Sanna, A., Szymczak, M., Moscadelli, L., van Langevelde, H. J., and Wolak, P.: 2020, *Astronomy & Astrophysics* **637**, A15

Bartkiewicz, A., Szymczak, M., and van Langevelde, H. J.: 2016, *Astronomy & Astrophysics* **587**, A104

Bate, M. R. and Bonnell, I. A.: 2005, *Monthly Notices of the Royal Astronomical Society* **356(4)**, 1201

Bayandina, O. S., Brogan, C. L., Burns, R. A., Chen, X., Hunter, T. R., Kurtz, S. E., MacLeod, G. C., Sobolev, A. M., Sugiyama, K., Val'tts, I. E., and Yonekura, Y.: 2022, *The Astronomical Journal* **163(2)**, 83

Beuther, H., Mottram, J. C., Ahmadi, A., Bosco, F., Linz, H., Henning, T., Klaassen, P., Winters, J. M., Maud, L. T., Kuiper, R., Semenov, D., Gieser, C., Peters, T., Urquhart, J. S., Pudritz, R., Ragan, S. E., Feng, S., Keto, E., Leurini, S., Cesaroni, R., Beltran, M., Palau, A., Sánchez-Monge, Á., Galvan-Madrid, R., Zhang, Q., Schilke, P., Wyrowski, F., Johnston, K. G., Longmore, S. N., Lumsden, S., Hoare, M., Menten, K. M., and Csengeri, T.: 2018, *Astronomy & Astrophysics* **617**, A100

Brandl, B., Sams, B. J., Bertoldi, F., Eckart, A., Genzel, R., Drapatz, S., Hofmann, R., Loewe, M., and Quirrenbach, A.: 1996, *The Astrophysical Journal* **466**, 254

Breen, S. L., Ellingsen, S. P., Contreras, Y., Green, J. A., Caswell, J. L., Stevens, J. B., Dawson, J. R., and Voronkov, M. A.: 2013, *Monthly Notices of the Royal Astronomical Society* **435(1)**, 524

Breen, S. L., Fuller, G. A., Caswell, J. L., Green, J. A., Avison, A., Ellingsen, S. P., Gray, M. D., Pestalozzi, M., Quinn, L. J., Richards, A. M. S., Thompson, M. A., and Voronkov, M. A.: 2015, *Monthly Notices of the Royal Astronomical Society* **450(4)**, 4109

Caswell, J. L., Vaile, R. A., and Ellingsen, S. P.: 1995, *Publications of the Astronomical Society of Australia* **12**, 37

Cesaroni, R., Felli, M., Testi, L., Walmsley, C. M., and Olmi, L.: 1997, *Astronomy & Astrophysics* **325**, 725

Cesaroni, R., Galli, D., Neri, R., and Walmsley, C. M.: 2014, *Astronomy & Astrophysics* **566**, A73

Cesaroni, R., Massi, F., Arcidiacono, C., Beltrán, M. T., McCarthy, D., Kulesa, C., Boutsia, K., Paris, D., Quirós-Pacheco, F., and Xompero, M.: 2013, *Astronomy & Astrophysics* **549**, A146

Cesaroni, R., Neri, R., Olmi, L., Testi, L., Walmsley, C. M., and Hofner, P.: 2005, *Astronomy & Astrophysics* **434(3)**, 1039

Clarke, A. J., Lumsden, S. L., Oudmaijer, R. D., Busfield, A. L., Hoare, M. G., Moore, T. J. T., Sheret, T. L., and Urquhart, J. S.: 2006, *Astronomy & Astrophysics* **457(1)**, 183–188

Cohen, M.: 1977, *The Astrophysical Journal* **215**, 533

Cragg, D. M., Sobolev, A. M., and Godfrey, P. D.: 2002, *Monthly Notices of the Royal Astronomical Society* **331(2)**, 521

Dale, J. E. and Davies, M. B.: 2006, *Monthly Notices of the Royal Astronomical Society* **366(4)**, 1424

De Buizer, J. M., Redman, R. O., Longmore, S. N., Caswell, J., and Feldman, P. A.: 2009, *Astronomy & Astrophysics* **493(1)**, 127

Elitzur, M.: 1992, *Astronomical masers*, Vol. 170, Springer Dordrecht

Fujisawa, K., Yonekura, Y., Sugiyama, K., Horiuchi, H., Hayashi, T., Hachisuka, K., Matsumoto, N., and Niinuma, K.: 2015, *The Astronomer's Telegram* **8286**, 1

Gieser, C., Beuther, H., Semenov, D., Ahmadi, A., Suri, S., Möller, T., Beltrán, M. T., Klaassen, P., Zhang, Q., Urquhart, J. S., Henning, T., Feng, S., Galván-Madrid, R., de Souza Magalhães, V., Moscadelli, L., Longmore, S., Leurini, S., Kuiper, R., Peters, T., Menten, K. M., Csengeri, T., Fuller, G., Wyrowski, F., Lumsden, S., Sánchez-Monge, Á., Maud, L., Linz, H., Palau, A., Schilke, P., Pety, J., Pudritz, R., Winters, J. M., and Piétu, V.: 2021, *Astronomy & Astrophysics* **648**, A66

Goedhart, S., Gaylard, M. J., and van der Walt, D. J.: 2004, *Monthly Notices of the Royal Astronomical Society* **355(2)**, 553

Gundermann, E. J.: 1965, *Ph.D. thesis*, Harvard University

Hu, B., Menten, K. M., Wu, Y., Bartkiewicz, A., Rygl, K., Reid, M. J., Urquhart, J. S., and Zheng, X.: 2016, *The Astrophysical Journal* **833(1)**, 18

Inayoshi, K., Sugiyama, K., Hosokawa, T., Motogi, K., and Tanaka, K. E. I.: 2013, *The Astrophysical Journal* **769(2)**, L20

Keimpema, A., Kettenis, M., Pogrebenko, S., Campbell, R., Cimó, G., Duev, D., Eldering, B., Kruithof, N., van Langevelde, H., Marchal, D., Molera Calvés, G., Ozdemir, H., Paragi, Z., Pidopryhora, Y., Szomoru, A., and Yang, J.: 2015, *Experimental Astronomy* **39(2)**, 259, VK: BIBCODE: 2015ExA....39..259K; DOI: 10.1007/s10686-015-9446-1; eprintid: arXiv:1502.00467

Lada, C. J.: 1987, in M. Peimbert and J. Jugaku (eds.), *Star Forming Regions*, Vol. 115, p. 1

Lada, C. J. and Wilking, B. A.: 1984, *The Astrophysical Journal* **287**, 610

Menten, K. M.: 1991, *The Astrophysical Journal Letters* **380**, L75

Moscadelli, L., Cesaroni, R., Rioja, M. J., Dodson, R., and Reid, M. J.: 2011, *Astronomy & Astrophysics* **526**, A66

Moscadelli, L., Sanna, A., Goddi, C., Walmsley, M. C., Cesaroni, R., Caratti o Garatti, A., Stecklum, B., Menten, K. M., and Kraus, A.: 2017, *Astronomy & Astrophysics* **600**, L8

Murakawa, K., Lumsden, S. L., Oudmaijer, R. D., Davies, B., Wheelwright, H. E., Hoare, M. G., and Ilee, J. D.: 2013, *Monthly Notices of the Royal Astronomical Society* **436(1)**, 511

Olech, M., Szymczak, M., Wolak, P., Sarniak, R., and Bartkiewicz, A.: 2019, *Monthly Notices of the Royal Astronomical Society* **486(1)**, 1236

Parfenov, S. Y. and Sobolev, A. M.: 2014, *Monthly Notices of the Royal Astronomical Society* **444(1)**, 620

Pestalozzi, M. R., Elitzur, M., and Conway, J. E.: 2009, *Astronomy & Astrophysics* **501(3)**, 999

Purcell, C.: 2007, Phd thesis, UNSW School of Physics, Example City, CA, Available at https://unsworks.unsw.edu.au/entities/publication/662a36a9-8538-461a-9066-afdc1cf385f6

Purser, S. J. D., Lumsden, S. L., Hoare, M. G., and Kurtz, S.: 2021, *Monthly Notices of the Royal Astronomical Society* **504(1)**, 338

Reid, M. J., Menten, K. M., Brunthaler, A., Zheng, X. W., Dame, T. M., Xu, Y., Li, J., Sakai, N., Wu, Y., Immer, K., and et al.: 2019, *The Astrophysical Journal* **885(2)**, 131

Scargle, J. D.: 1982, *The Astrophysical Journal* **263**, 835

Shimoikura, T., Kobayashi, H., Omodaka, T., Diamond, P. J., Matveyenko, L. I., and Fujisawa, K.: 2005, *The Astrophysical Journal* **634(1)**, 459

Slysh, V. I., Val'tts, I. E., Kalenskii, S. V., Voronkov, M. A., Palagi, F., Tofani, G., and Catarzi, M.: 1999, *Astronomy and Astrophysics Supplement Series* **134**, 115

Slysh, V. I., Voronkov, M. A., Val'tts, I. E., and Migenes, V.: 2002, *Astronomy Reports* **46(12)**, 969

Stetson, P. B.: 1996, *Publications of the Astronomical Society of the Pacific* **108**, 851

Sugiyama, K., Yonekura, Y., Motogi, K., Saito, Y., Momose, M., Honma, M., Hirota, T., Uchiyama, M., Tanaka, K. E. I., Kramer, B. H., Asanok, K., Jaroenjittichai, P., and Fujisawa, K.: 2019, *Journal of Physics: Conference Series* **1380(1)**, 012057

Surcis, G., Vlemmings, W. H. T., van Langevelde, H. J., Moscadelli, L., and Hutawarakorn Kramer, B.: 2014, *Astronomy & Astrophysics* **563**, A30

Szymczak, M., Hrynek, G., and Kus, A. J.: 2000, *Astron. Astrophys. Suppl. Ser.* **143(2)**, 269

Szymczak, M., Olech, M., Sarniak, R., Wolak, P., and Bartkiewicz, A.: 2017, *Monthly Notices of the Royal Astronomical Society* **474(1)**, 219

Szymczak, M., Olech, M., Wolak, P., Bartkiewicz, A., and Gawroński, M.: 2016, *Monthly Notices of the Royal Astronomical Society* **459(1)**, L56–L60

Szymczak, M., Wolak, P., and Bartkiewicz, A.: 2015, *Monthly Notices of the Royal Astronomical Society* **448(3)**, 2284

Szymczak, M., Wolak, P., Bartkiewicz, A., and Borkowski, K. M.: 2012, *Astronomische Nachrichten* **333(7)**, 634

Szymczak, M., Wolak, P., Bartkiewicz, A., and van Langevelde, H. J.: 2011, *Astronomy & Astrophysics* **531**, L3

Uchiyama, M., Yamashita, T., Sugiyama, K., Nakaoka, T., Kawabata, M., Itoh, R., Yamanaka, M., Akitaya, H., Kawabata, K., Yonekura, Y., Saito, Y., Motogi, K., and Fujisawa, K.: 2019, *Publications of the Astronomical Society of Japan* 72(1), 4

Val'tts, I. E., Slysh, V. I., Voronkov, M. A., and Migenes, V.: 2002, *ASP Conference Proceedings* **279**, 279

van der Walt, D. J.: 2011, *The Astronomical Journal* **141(5)**, 152

van der Walt, D. J., Sobolev, A. M., and Butner, H.: 2007, *Astronomy & Astrophysics* **464(3)**, 1015

Vlemmings, W. H. T., Surcis, G., Torstensson, K. J. E., and van Langevelde, H. J.: 2010, *Monthly Notices of the Royal Astronomical Society* **404(1)**, 134

Vorobyov, E. I. and Basu, S.: 2006, *The Astrophysical Journal* **650(2)**, 956

Šteinbergs, J., Aberfelds, A., Bleiders, M., and Shmeld, I.: 2021, *Astronomical and Astrophysical Transactions* **32(3)**, 227

Weinreb, S., Meeks, M. L., and Carter, J. C.: 1965, Nature **208(5009)**, 440

Winkel, B., Kraus, A., and Bach, U.: 2012, *Astronomy & Astrophysics* **540**, A140

Yang, K., Chen, X., Shen, Z.-Q., Li, X.-Q., Wang, J.-Z., Jiang, D.-R., Li, J., Dong, J., Wu, Y.-J., and Qiao, H.-H.: 2019, *Astrophysical Journal Supplement Series* **241(2)**, 18

Zinnecker, H. and Yorke, H. W.: 2007, *Annual Review of Astronomy and Astrophysics* **45(1)**, 481